First Superheavy Element Experiments at the GSI Recoil Separator TASCA: The Production and Decay of Element 114 in the 244Pu(48Ca,3-4n) Reaction

Gates, J. M.; Duellmann, Ch E.; Schaedel, M.; Yakushev, A.; Tuerler, A.; Eberhardt, K.; Kratz, J. V.; Ackermann, D.; Andersson, L. -L.; Block, M.; Bruechle, W.; Dvorak, J.; Essel, H. G.; Ellison, P. A.; Even, J.; Forsberg, Ulrika; Gellanki, Jnaneswari; Gorshkov, A.; Graeger, R.; Gregorich, K. E.; Hartmann, W.; Herzberg, R. -D.; Hessberger, F. P.; Hild, D.; Huebner, A.; Jaeger, E.; Khuyagbaatar, J.; Kindler, B.; Krier, J.; Kurz, N.; Lahiri, S.; Liebe, D.; Lommel, B.; Maiti, M.; Nitsche, H.; Omtvedt, J. P.; Parr, E.; Rudolph, Dirk; Runke, J.; Schaffner, H.; Schausten, B.; Schimpf, E.; Semchenkov, A.; Steiner, J.; Thoerle-Pospiech, P.; Uusitalo, J.; Wegrzecki, M.; Wiehl, N.

Published in:
Physical Review C (Nuclear Physics)

DOI:
10.1103/PhysRevC.83.054618

2011

First superheavy element experiments at the GSI recoil separator TASCA: The production and decay of element 114 in the ^{244}Pu(^{48}Ca,3-4n) reaction

J. M. Gates,[1,2,3,*] Ch. E. Düllmann,[1,4,5] M. Schädel,[1] A. Yakushev,[2] A. Türler,[2,†] K. Eberhardt,[4] J. V. Kratz,[4] D. Ackermann,[1] L.-L. Andersson,[6] M. Block,[1] W. Brüchle,[1] J. Dvorak,[3] H. G. Essel,[1] P. A. Ellison,[3,7] J. Even,[4] U. Forsberg,[8] J. Gellanki,[8] A. Gorshkov,[2] R. Graeger,[2] K. E. Gregorich,[3] W. Hartmann,[1] R.-D. Herzberg,[6] F. P. Heßberger,[1] D. Hild,[4] A. Hübner,[1] E. Jäger,[1] J. Khuyagbaatar,[1] B. Kindler,[1] J. Krier,[1] N. Kurz,[1] S. Lahiri,[9] D. Liebe,[4] B. Lommel,[1] M. Maiti,[9] H. Nitsche,[3,7] J. P. Omtvedt,[10] E. Parr,[6] D. Rudolph,[8] J. Runke,[4] H. Schaffner,[1] B. Schausten,[1] E. Schimpf,[1] A. Semchenkov,[10] J. Steiner,[1] P. Thörle-Pospiech,[4] J. Uusitalo,[11] M. Wegrzecki,[12] and N. Wiehl[4]

[1]*GSI Helmholtzzentrum für Schwerionenforschung GmbH, D-64291 Darmstadt, Germany*
[2]*Technische Universität München, D-85748 Garching, Germany*
[3]*Lawrence Berkeley National Laboratory, Berkeley, California 94720-8169, USA*
[4]*Johannes Gutenberg-Universität Mainz, D-55099 Mainz, Germany*
[5]*Helmholtz Institute Mainz, D-55099 Mainz, Germany*
[6]*University of Liverpool, Liverpool L69 7ZE, United Kingdom*
[7]*University of California, Berkeley, California 94720-1460, USA*
[8]*Lund University, SE-22100 Lund, Sweden*
[9]*Saha Institute of Nuclear Physics, Kolkata-700064, India*
[10]*University of Oslo, NO-0315 Oslo, Norway*
[11]*University of Jyväskylä, FI-40014 Jyväskylä, Finland*
[12]*Institute of Electron Technology, PL-02-668 Warsaw, Poland*

(Received 13 December 2010; revised manuscript received 31 March 2011; published 27 May 2011)

Experiments with the new recoil separator, Transactinide Separator and Chemistry Apparatus (TASCA), at the GSI were performed by using beams of ^{48}Ca to irradiate targets of $^{206-208}$Pb, which led to the production of $^{252-254}$No isotopes. These studies allowed for evaluation of the performance of TASCA when coupled to a new detector and electronics system. By following these studies, the isotopes of element 114 ($^{288-291}$114) were produced in irradiations of ^{244}Pu targets with ^{48}Ca beams at compound nucleus excitation energies around 41.7 and 37.5 MeV, demonstrating TASCA's ability to perform experiments with picobarn-level cross sections. A total of 15 decay chains were observed and were assigned to the decay of $^{288-291}$114. A new α-decay branch in ^{281}Ds was observed, leading to the new nucleus ^{277}Hs.

DOI: 10.1103/PhysRevC.83.054618 PACS number(s): 25.70.Jj, 27.90.+b, 29.30.Aj

I. INTRODUCTION

The Transactinide (TAN) Separator and Chemistry Apparatus (TASCA) is a recently installed recoil separator at the GSI Helmholtzzentrum für Schwerionenforschung (GSI) in Darmstadt, Germany [1]. It was optimized for the study of neutron-rich TAN ($Z \geqslant 104$) elements produced in hot fusion reactions between highly intense ion beams and actinide targets. Because of production rates on the order of nano- ($Z = 104$) to femtobarns ($Z = 113$ [2]), TASCA was designed to (i) separate the TAN of interest from the beam and plethora of unwanted reaction products and (ii) maximize the transmission of TANs from the target to the focal plane of TASCA, while suppressing transmission of the beam and unwanted reaction products. By doing this, it is then possible to perform chemical investigations, nuclear structure and nuclear reaction studies of the most neutron-rich nuclides.

TASCA was commissioned by using reactions with nanobarn or larger cross sections [3,4]. Therefore, the extension of TASCA experiments to picobarn-level cross sections remained the final step in the commissioning phase. To investigate a reaction with picobarn-level cross sections, a new detection and electronics system was developed for TASCA [5]. As one of the first crucial tests of the performance of this system, when coupled to TASCA, we chose to investigate the 2n exit channels of ^{48}Ca-induced reactions on $^{206-208}$Pb to produce $^{252-254}$No. These reactions have cross sections on the order of microbarns [6], which leads to expected production rates of atoms per second. These reactions have also been extensively studied at several recoil separators including the Berkeley Gas-filled Separator (BGS) [7–9], the Dubna Gas-Filled Recoil Separator (DGFRS) [6], the gas-filled Recoil Ion Transport Unit (RITU) [10], the Fragment Mass Analyzer (FMA) [11], the velocity-filter Separator for Heavy Ion reaction Products (SHIP) [12–14], and the energy-filter VASSILISSA [15]. This allows for a comparison of the cross sections measured at TASCA to those measured at other recoil separators, which gives an indication of the efficiency of TASCA for these reactions. Decay properties of $^{252-254}$No include α-decay, spontaneous fission (SF), and electron capture branches,

*Electronic address: jmgates@lbl.gov
†Present address: Paul Scherrer Institute and University of Bern, CH-5232 Villigen, Switzerland.

which allow for the characterization of the detection and data acquisition system using multiple different decay scenarios. In addition, α decays of ^{253}No are in prompt coincidence with three intense γ lines [16], ideal for testing TASCA's ability to be used in nuclear structure studies [17].

After establishing the new detection setup coupled to TASCA for the ^{48}Ca + $^{206-208}$Pb reactions, an extension of TASCA commissioning experiments toward reactions that have lower production rates was undertaken. For this purpose, the ^{244}Pu(^{48}Ca,3-4n)^{289,288}114 reaction, with a published cross section of $1.7^{+2.5}_{-1.1}$ and $5.3^{+3.6}_{-2.1}$ pb for the 3 and 4n exit channels [18], respectively, was investigated. The 3n exit channel of this reaction was reported in 1999 when a collaboration working at the DGFRS published a decay chain assigned to the observation of ^{289}114, an α-particle emitter with a half-life $t_{1/2}$ of 21 s [19]. Among the ^{289}114 daughters were the isotopes ^{285}Cn and ^{281}Ds, which were observed to decay via α-particle emission with lifetimes τ of 15.4 min and 1.6 min, respectively. The chain terminated in SF of ^{277}Hs 16.5 min later. Shortly following this, reports of the production of ^{288}114 in the ^{244}Pu(^{48}Ca,4n) reaction were published [20]. When ^{288}114 was observed as the α-decay daughter of the new isotope ^{292}116, as produced in the ^{248}Cm(^{48}Ca,4n) reaction, these reports were seemingly substantiated [21]. However, more recent work from the DGFRS, which produced additional and more detailed data, led to reassigning decay chains that were originally attributed to ^{288}114. They are now ascribed to ^{289}114 [18], while the ^{289}114 decay chain [19] was not reproduced. Further studies at the DGFRS, which used the ^{242}Pu(^{48}Ca,3-4n)^{287,286}114 and ^{244}Pu(^{48}Ca,3-4n)^{289,288}114 reactions led to new types of decay chains, which were assigned to ^{286}114, ^{287}114 [22], and ^{288}114 [18]. The current body of acquired DGFRS data interpreted by the DGFRS group is summarized in Ref. [23].

In 2009, the ^{48}Ca + ^{242}Pu reaction was studied at the BGS [24]. One atom of ^{287}114, produced in the 3n evaporation channel, and one atom of ^{286}114, produced in the 4n evaporation channel, were observed. These results provided the confirmation of the production of decay patterns assigned to element 114, as well as a confirmation of the decay properties assigned to ^{286,287}114. The original reported cross sections were $1.4^{+3.2}_{-1.2}$ pb each but were later revised to $3.1^{+4.9}_{-2.6}$ pb [25], in agreement with cross sections reported by Oganessian *et al.* [22]. We undertook investigating the ^{244}Pu(^{48}Ca,3-4n)^{289,288}114 reactions with the goal of (i) demonstrating the ability of TASCA to perform experiments with picobarn-level cross sections and (ii) providing a confirmation of the production of element 114 with ^{244}Pu targets and ^{48}Ca beams. Here, we report on results of test experiments with ^{48}Ca beams and $^{206-208}$Pb targets, present an extended discussion of the experimental setup, and include additional results on the ^{48}Ca + ^{244}Pu reaction, part of which was previously published in Ref. [26].

II. EXPERIMENTAL

A pulsed (5 ms on/15 ms off) beam of ^{48}Ca^{10+} was extracted from an electron cyclotron resonance (ECR) ion source and was accelerated by the universal linear accelerator

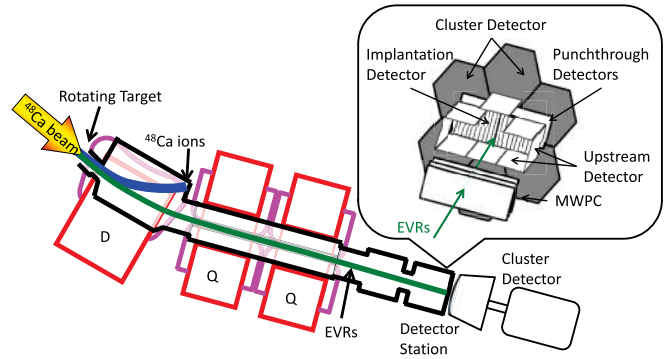

FIG. 1. (Color online) Layout of TASCA and the detector setup. *D* is a dipole magnet, and *Q* is a quadrupole magnet. The figure is not to scale.

(UNILAC) at the GSI to laboratory-frame energies of 231.2, 254.6, and 259.4 MeV. The beam passed through an induction coil prior to the entrance of TASCA to measure the beam intensity in a nondestructive way. A schematic of the TASCA setup is shown in Fig. 1. The vacuum of the beamline was separated from the 80-Pa helium gas in TASCA by using a windowless three-stage differential pumping system. For portions of the 259.4-MeV run and the entire 254.6-MeV run, a 55-μg cm^{-2}-thick carbon stripper foil was mounted directly upstream of the target to increase the charge state of the beam. During these irradiations, the beam energy was increased to compensate for the energy loss inside the stripper foil. The beam then passed through a (2.22 $\pm$ 0.05)-μm-thick Ti-target backing before entering the targets. Three arc-shaped target segments were mounted on a target wheel, which rotated synchronously with the beam macrostructure. For the 231.2-MeV irradiation, targets with average thicknesses of 558-μg cm^{-2} ^{206}PbS, 522-μg cm^{-2} ^{207}PbS, and 531-μg cm^{-2} ^{208}PbS were used. All PbS targets were covered with 10-μg cm^{-2} $^{\text{nat}}$C. At ^{48}Ca beam energies of 259.4 and 254.6 MeV from the UNILAC, ^{244}PuO$_2$ targets (isotopic composition: 97.9% ^{244}Pu, 1.3% ^{242}Pu, 0.7% ^{240}Pu, and <0.1% other) were irradiated. A summary of the experiments, beam energies, and doses can be found in Table I. The ^{244}PuO$_2$ targets were prepared on (2.22 $\pm$ 0.05)-μm-thick Ti foils by electrochemical deposition from isobutanolic solution [27], a procedure that yielded the oxide form after annealing. Over the course of the experiment, four ^{244}Pu target segments with a beam-dose-weighted-average target thickness of 438-μg cm^{-2} ^{244}Pu (as 495-μg cm^{-2} ^{244}PuO$_2$) were irradiated with typical beam intensities of 2 $\times$ 10^{12} particles s^{-1}.

Energy losses in carbon, titanium, and lead sulfide ($^{206-208}$PbS) were calculated with SRIM2008 [28]. Beam energies inside the ^{207,208}PbS targets were 212.3–217.0 MeV. Inside the ^{206}PbS target, the beam energy range was 212.0–217.0 MeV. Compound nucleus excitation energies were calculated by using beam energies with experimental mass defects for ^{48}Ca, $^{206-208}$Pb, and $^{252-254}$No [29]. Excitation energy ranges inside the targets were 21.2 $\pm$ 2.0, 20.7 $\pm$ 1.9, and 20.5 $\pm$ 1.9 MeV for ^{206}PbS, ^{207}PbS, and ^{208}PbS, respectively, where the error bars represent the range of excitation energies

TABLE I. List of experiments with ^{48}Ca beams included in this paper.

Target	Exit channel	Product	E^* (MeV)	E_{beam} (MeV)	TASCA mode	$B\rho$ (T m)	Beam dose ($\times 10^{16}$)	ε_{TASCA}[a] (%)	Cross section[a]	Cross section from literature[b]
^{206}Pb	2n	^{252}No	21.2 ± 2.0	231.2	HTM	2.10	10.0	56 ± 6	(310 ± 10) nb	SHIP: (430 ± 10) nb [13] DGFRS: (500 ± 40) nb [6]
^{206}Pb	2n	^{252}No	21.2 ± 2.0	231.2	HTM	2.22	0.9			
^{206}Pb	2n	^{252}No	21.2 ± 2.0	231.2	HTM	1.98	1.3			
^{207}Pb	2n	^{253}No	20.7 ± 1.9	231.2	HTM	2.10	3.9	56 ± 6	(760 ± 10) nb	DGFRS: (1130 ± 170) nb [6]
^{208}Pb	2n	^{254}No	20.5 ± 1.9	231.2	HTM	2.10	1.4	56 ± 6	(1890 ± 40) nb	BGS: (2250 ± 380) [8]
^{208}Pb	2n	^{254}No	20.5 ± 1.9	231.2	SIM	2.10	1.3	40 ± 4	(1650 ± 40) nb	DGFRS: (2370 ± 180) [6] SHIP: (1760 ± 60) [12–14,42] VASSILISSA: (1920 ± 260) [15]
^{244}Pu	3n	^{289}114	$41.7^{+2.2}_{-1.9}$	259.4	HTM	2.23	244	60 ± 6	$3.5^{+3.3}_{-2.0}$ pb	
^{244}Pu	3n	^{289}114	$37.5^{+2.0}_{-1.4}$	254.6	HTM	2.28	115	59 ± 6	$8.0^{+7.4}_{-4.5}$ pb	DGFRS: $1.7^{+2.5}_{-1.1}$ pb
^{244}Pu	3n	^{289}114	$41.7^{+2.2}_{-1.9}$	259.4	SIM	2.28	100	35 ± 4	<27 pb [c]	
^{244}Pu	4n	^{288}114	$41.7^{+2.2}_{-1.9}$	259.4	HTM	2.23	244	60 ± 6	$9.8^{+3.9}_{-3.1}$ pb	
^{244}Pu	4n	^{288}114	$37.5^{+2.0}_{-1.4}$	254.6	HTM	2.28	115	59 ± 6	$2.8^{+4.2}_{-2.1}$ pb	DGFRS: $5.3^{+3.6}_{-2.1}$ pb
^{244}Pu	4n	^{288}114	$41.7^{+2.2}_{-1.9}$	259.4	SIM	2.28	100	35 ± 4	11^{+15}_{-7} pb	

[a] ε_{TASCA} and cross sections were not calculated for ^{206}Pb(^{48}Ca,2n)^{252}No at $B\rho$ settings of 2.22 and 1.98 T m as the products were not centered in the FPD.
[b] Cross sections for the $^{206-208}$Pb(^{48}Ca,2n)$^{252-254}$No reactions are reported at the maximum of a fit to available data as described in Sec. III C2.
[c] Upper limit based on a 95% confidence interval.

within the targets. Energy losses inside the $^{244}PuO_2$ were extrapolated from values calculated with SRIM2008 of ^{48}Ca in hypothetical $^{244}RnO_2$, $^{244}RaO_2$, $^{244}ThO_2$, and $^{244}UO_2$ to $^{244}PuO_2$. Beam energies inside the $^{244}PuO_2$ target material were initially 241.3–246.2 MeV and then later were decreased to 236.4–241.0 MeV. Compound nucleus excitation energies were calculated by using beam energies with experimental mass defects for ^{48}Ca and ^{244}Pu [29] and Thomas-Fermi mass defects for the compound nucleus [30]. Resulting ranges of compound nucleus excitation energies within the $^{244}PuO_2$ targets were $41.7^{+2.2}_{-1.9}$ and $37.5^{+2.0}_{-1.4}$ MeV, where 41.7 and 37.5 represent the excitation energy at the beam-dose-weighted center of the target, and the error bars represent the average spread in energies in the target.

Compound nucleus evaporation residues (EVRs) are formed with the momentum of the beam and recoil out of the target and into TASCA. TASCA comprises a DQQ magnet configuration, where D denotes a dipole magnet and Q denotes a quadrupole magnet [1]. EVRs were separated from the beam and other unwanted reaction products in TASCA based upon their differing magnetic rigidities $B\rho$ in the 80-Pa helium gas. For the 231.2-MeV irradiation of the $^{206-208}$Pb targets, TASCA was set to center EVRs of 2.10 T m in the focal plane. When ^{206}Pb targets were irradiated, $B\rho$ settings of 2.22 and 1.98 T m were also used to move the implantation of SF-decaying ^{252}No EVRs to the edges of the detector. For the first part of the element 114 run, at 259.4 MeV, magnetic rigidities of the element 114 EVRs were estimated as described in Ref. [7], and accordingly, TASCA was set to center EVRs with a $B\rho$ of 2.23 T m in the focal plane. After observation of the position of the first ten events, the centered $B\rho$ was increased to 2.28 T m.

TASCA is designed to be operated with the quadrupole magnets polarized either as $Q_V Q_H$ or $Q_H Q_V$, where the indices indicate vertical (V) or horizontal (H) focusing [1]. This allows for choosing between two different focal-plane image sizes, each with different EVR transmission efficiencies. When polarized as $Q_H Q_V$, the efficiency of TASCA ε_{TASCA} for the transmission of EVRs to the focal plane is increased, and the focal-plane image is more dispersed. For the majority of the run, TASCA was operated in this high transmission mode (HTM) to maximize the rate of 114 events. However, for part of the run, TASCA was operated in the $Q_V Q_H$ configuration, referred to as the small image mode (SIM). In this mode, the focal-plane image is significantly smaller than in the HTM, which comes at the cost of reduced EVR transmission efficiency. The use of SIM was performed to determine the feasibility of future experiments on the chemistry of element 114.

A. TASCA efficiency

ε_{TASCA} is limited by (i) the initial position, energy, and angular distribution of recoils that exit the target, and (ii) the transmission of these recoils through TASCA. The latter is limited by the influence of the magnetic fields on the recoils, as well as their energy loss, multiple scattering, and charge exchange in the He-fill gas. All of these effects, together with the effects of the estimated angular and energy distributions of the ^{48}Ca beam that enters TASCA were calculated with a Monte Carlo simulation developed for the BGS and later adapted for TASCA [7,31,32]. In this simulation, the initial ^{48}Ca beam energies and directions were chosen from assumed Gaussian energy and Gaussian angular distributions. The Gaussian energy distributions for the ^{244}Pu irradiation had a full width at half maximum (FWHM) of 0.2% (a typical beam

energy uncertainty from the UNILAC) and centroids c of 243.8 and 238.7 MeV for the 259.4- and 254.6-MeV irradiations, respectively, chosen to put c at the center of the targets with an estimated σs of 4 MeV for both irradiations. The Gaussian angular distributions had a FWHM $= 0.9°$—typical for the beamline that leads to TASCA. The beam energy was corrected for energy loss in the target backings. Points were randomly chosen from the assumed Gaussian excitation function with centroids positioned at the center-of-target beam energies. Variation in both backing and target thickness were taken into account using assumed thickness distributions approximated by the shape of a house with a peaked roof. If those points were within the energy range subtended by the target [thickness $=$ (495 ± 50)-μg/cm^2 $^{244}PuO_2$, $dE/dx = 8.3$ MeV mg^{-1} cm^2], the depth of interaction in the target was calculated, and a simulation of the trajectory of an EVR was initiated. The initial energy and angle of the EVR in the laboratory frame were corrected for the effect of isotropic (center-of-mass frame) evaporation of three or four neutrons, with the assumption that each neutron is emitted with 2 MeV of kinetic energy. Energy loss and angular scattering in the remaining target material were calculated for each EVR by using SRIM2008 [28]. After exiting the target, trajectories through TASCA were simulated, which included effects of magnetic fields, charge exchange in the gas [7], scattering in the gas [33], and energy loss in the gas [28]. By comparing the number of EVRs that reach the focal-plane detector in the simulation with the initial number of ^{48}Ca beam particles, effects of the fraction of the excitation function contained in the target and of $\varepsilon_{\mathrm{TASCA}}$ as a function of target depth were accounted for. Figure 2 contains horizontal and vertical cross-sectional views of predicted element 114 EVR trajectories inside TASCA during HTM operation. $\varepsilon_{\mathrm{TASCA}}$ is estimated to be $(60 \pm 6)\%$, $(59 \pm 6)\%$, and $(35 \pm 4)\%$ for the 259.4-MeV HTM, 254.6-MeV HTM, and 259.4-MeV SIM runs, respectively. Beam doses of 2.44×10^{18} (259.4-MeV HTM run), 1.15×10^{18} (254.6-MeV HTM run), and 1.00×10^{18} (259.4-MeV SIM run) particles were acquired. The uncertainty in the beam dose is 9% and is described in more detail in Sec. III F. Similar calculations were performed for irradiations of the $^{206-208}$Pb targets, and $\varepsilon_{\mathrm{TASCA}}$ was estimated to be $(56 \pm 6)\%$ for the $^{206-208}$Pb(^{48}Ca,$2n$) reactions. $\varepsilon_{\mathrm{TASCA}}$ values for all of the experiments in this paper can be found in Table I.

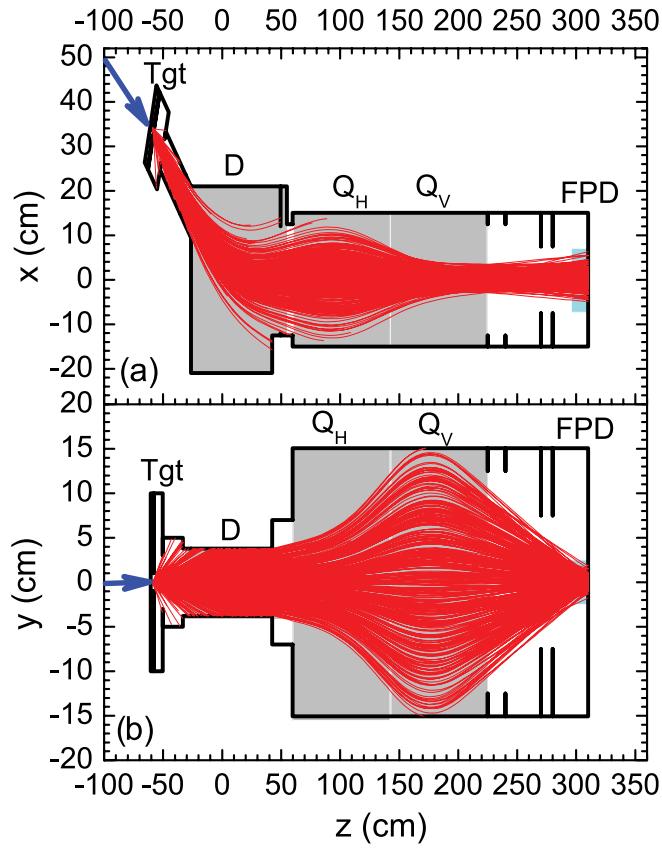

FIG. 2. (Color online) (a) Horizontal and (b) vertical cross-sectional views of expected element 114 EVR trajectories inside of TASCA for HTM. The thick line is a representation of the TASCA vacuum chambers inside the magnets where D is the dipole magnet and Q_{H} and Q_{V} are the horizontally and vertically focusing quadrupole magnets, respectively. FPD and Tgt indicate the positions of the focal plane detector and target, respectively. The labels on the axes are the distance (in centimeters) from the center of the dipole chamber in TASCA as defined in the Monte Carlo simulation. They are skewed to better show trajectories of individual particles. The beam enters TASCA from the left, passing through the center of the target area, as shown by the arrows. The predicted element 114 EVR trajectories are curved lines filling TASCA.

B. Detection setup

After separation in the TASCA, the element 114 EVRs passed through a multiwire proportional counter (MWPC) and were implanted into a focal-plane detector (FPD). The MWPC was located ~27-cm upstream of the FPD and consisted of two 0.25-μm-thick Mylar windows, which isolated an isobutane-filled gas, held at a pressure of 400 Pa. No time-to-amplitude converter was used to give timing information between the MWPC and the FPD. The output signal from the MWPC was divided after a preamplifier in two: (i) from one, a logical signal was created by using a timing filter amplifier and a constant fraction discriminator; (ii) the other one was amplified by a spectrometric amplifier and was digitalized in an analog-to-digital converter (ADC). Both the logical signal and the digitalized amplitude were read out as part of the event triggered by any signal from the FPD and were used to allow for differentiation between implantation events and decays within the FPD.

The FPD was composed of an implantation detector (ID) and an upstream detector. The ID consisted of two 300-μm-thick, 72 $\times$ 48-mm^2 double-sided silicon strip detectors (DSSSDs). The front side of each DSSSD contained 72 vertical strips with a 1-mm pitch and 900-μm-wide strips thereby giving the position of the events along the X axis (hereafter referred to as the StopX strips). The back side of the DSSSD consisted of 48 horizontal strips with a 1-mm pitch and 500-μm-wide strips, giving the position of the events along the Y axis (hereafter referred to as the StopY strips). Overall, the ID composed 144 vertical strips and 48 horizontal strips. The geometric efficiency of the DSSSD for registering events, which were implanted into the detector with both X and Y

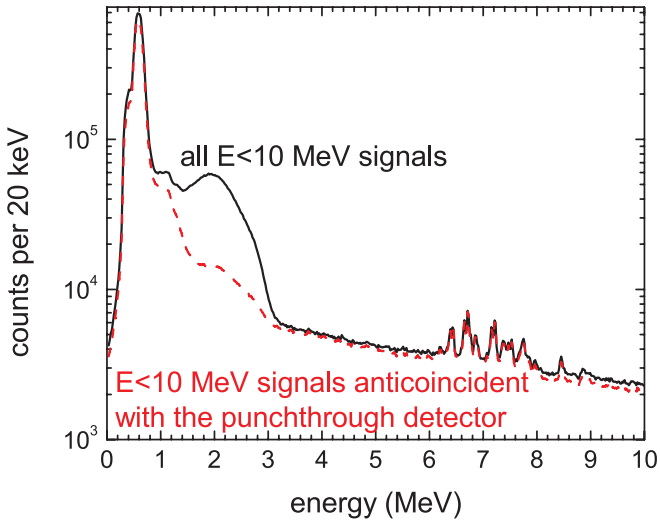

FIG. 3. (Color online) Spectra of (solid line) all data with $E <$ 10 MeV from the 259.4-MeV HTM run and (dashed line) all data with $E <$10 MeV that were anticoincident with a signal from the punch-through detector.

coordinates, was 90% [5]. To discriminate decaylike events (events anticoincident with a signal from the MWPC) from signals caused by light and low-ionizing particles (e.g., H^+, He^+, and He^{2+} from interactions of the beam with the He-fill gas), which pass through the MWPC undetected and deposit a similar amount of energy in the FPD, two 500-μm-thick, 72 $\times$ 48-mm^2 single-sided silicon strip detectors (SSSSDs) were mounted directly behind the ID. A signal in any of these punch-through detectors indicates light and low-ionizing particles. Figure 3 contains spectra of all events with $E <$ 10 MeV during the 259.4-MeV HTM run as well as events with $E <$ 10 MeV during the 259.4-MeV HTM run that were anticoincident with the punch-through detectors. As can be seen in the figure, the punch-through detectors provided background suppression mainly in the region of 1–3 MeV, which is the typical energy deposited in 300-μm-thick silicon by light and low-ionizing particles.

Eight additional 500-μm-thick, 72 $\times$ 48-mm^2 SSSSDs were mounted perpendicular to, and upstream of, the ID to form a five-sided box configuration as shown in Fig. 1. Each SSSSD had eight 5.75-mm-wide strips with a 6-mm pitch. These upstream detectors allowed for detecting α particles and SF fragments that escaped from the ID, thus, significantly enhancing the α-particle detection efficiency and allowing for registering the full energy of both fragments of SF events. Data acquisition was triggered by any event that registered more than ~300 keV in a DSSSD or more than ~500 keV in a SSSSD. The efficiency for detecting α particles was 72% of 4π. Fifty percent of all α particles deposit their full energy in the ID. An additional 22% of α particles lose a fraction of their energy in the ID and hit an upstream detector. Thus, their full energy can be reconstructed by summing the signals in both the implantation and the upstream detectors. Of the remaining 28% of all α particles, most escape out of the front of the detector box at an angle that leads to deposition of 300–500 keV in the FPD caused by a shallow implantation depth and the 0.6-μm dead layer on the detectors. The FPD was calibrated in the absence of the beam with an external four-line α-particle source (^{148}Gd, ^{239}Pu, ^{241}Am, and ^{244}Cm). The calibration was monitored online during the 254.6- and 259.4-MeV runs using α decays from the implanted transfer reaction products (TRPs) ^{214g}Fr (α-particle energy $E_\alpha =$ 8427 keV) and ^{212m}Po ($E_\alpha =$ 11 650 keV).

Because of the spacing between StopY strips of the ID, ~13%–20% of events (depending on energy) were split between two neighboring StopY strips. Energy splitting between neighboring StopX strips was only observed in 0.008% of events. To be considered correlated, all events within a decay chain were required to be in the same StopX strip and either in the same StopY strip or split between the same two neighboring StopY strips, hereafter referred to as a pixel.

One germanium cluster detector [34] with seven independent germanium crystals was mounted behind the 3-mm-thick Al back plate of the TASCA detection chamber such that the germanium crystals were positioned about 2 cm behind the ID. A standard ^{152}Eu γ-ray source was used for γ-ray energy calibrations. The α-γ coincidence source ^{241}Am, as well as α-γ coincidences following the ^{207}Pb(^{48}Ca,2n)^{253}No reaction were used to produce prompt α-γ correlations between the FPD electronics and the eight-channel sampling ADC used to process the germanium-detector signals.

The status of the beam pulse (BP) (whether the beam was or was not being delivered to TASCA) was recorded by a flag in each event in the data, which provided no information on the time since the start (or stop) of the BP. As such, there was an inherent uncertainty in the time each BP began and ended proportional to 1/(data rate). The UNILAC delivers BPs at a rate of 50 Hz (sometimes an experiment gets <50 Hz because of beam sharing), which means that a new BP should begin 20 ms after the start of the preceding pulse. The actual time difference between the start of individual BPs varies by up to 0.1% in an unpredictable manner. Due to this and the number of BPs required to obtain statistics (approximately ten events are implanted in the FPD during each 5-ms BP), the beginning of an individual BP could not be estimated within <100 μs.

C. Correlation search conditions

Decay properties of $^{252-254}$No and their daughters $^{248-250}$Fm are well known [35]. ^{252}No (α-branching ratio $B_\alpha = 0.731$: $E_\alpha = 8.42$, α-particle intensity $I_\alpha = 0.25$; $E_\alpha =$ 8.37 MeV, $I_\alpha = 0.75$; $B_{SF} = 0.269$, $t_{1/2} = 2.30$ s [35]) and its daughter ^{248}Fm ($B_\alpha = 0.93$: $E_\alpha = 7.87$, $I_\alpha = 0.8$; $E_\alpha =$ 7.83 MeV, $I_\alpha = 0.2$; $t_{1/2} = 36$ s [35]) are both short-lived isotopes with significant α-decay branches. ^{252}No also has a significant SF-branching ratio. This allowed for the use of four semi-independent methods of calculating the amount of ^{252}No in the FPD:

(i) Integral of ^{252}No-like α particles [$8.25 < E_\alpha$ (MeV) $<$ 8.55].

(ii) EVR-α correlations consisting of an EVR [$5.0 < E_{EVR}$ (MeV) < 12.0, coincident with the BP and the MWPC] followed within 6.9 s (three times the 2.3-s ^{252}No half-life)

TABLE II. Search conditions for decay chains, all energies are in MeV.

Isotope	Chain type	Number of chain member			
		1	2	3	4
^{252}No	α only	α: $8.25 < E_\alpha < 8.55$[b]			
	EVR-α	EVR: $[5.0 < E_{\rm EVR} < 12.0]$[a]	α: $8.25 <$; $E_\alpha < 8.55$[b] $\Delta t_{EVR-\alpha-\alpha} < 6.9$ s		
	EVR-α-α	EVR: $[5.0 < E_{\rm EVR} < 12.0]$[a]	α: $8.25 < E_\alpha < 8.55$[b] $\Delta t_{EVR-\alpha} < 6.9$ s	α: $7.7 < E_\alpha < 7.95$[b] $\Delta t_{\alpha-\alpha} < 108$ s	
	EVR-SF	EVR: $[5.0 < E_{\rm EVR} < 12.0]$[a]	SF: $80 < E_{\rm SF} < 300$[b] $E_{\rm ID} < 200$ MeV $\Delta t_{\rm EVR-SF} < 6.9$ s		
^{253}No	α only	α: $7.85 < E_\alpha < 8.25$[b]			
^{254}No	α only	α: $7.85 < E_\alpha < 8.25$[b]			
^{288}114	EVR-α-SF	EVR: $[3.0 < E_{\rm EVR} < 15.0]$[a]	α: $9.7 < E_\alpha < 10.2$ $\Delta t_{EVR-\alpha} < 7$ s	SF: $80 < E_{\rm SF} < 300$ $E_{\rm ID} < 200$ MeV $\Delta t_{\alpha-SF} < 1$ s	
^{289}114	EVR-α-α-SF	EVR: $[3.0 < E_{\rm EVR} < 15.0]$[a]	α: $9.7 < E_\alpha < 10.2$ $\Delta t_{EVR-\alpha} < 7$ s	α: $9.0 < E_\alpha < 9.5$ $\Delta t_\alpha - \alpha < 150$ s	SF: $80 < E_{\rm SF} < 300$ $E_{\rm ID} < 200$ $\Delta t_{\alpha-SF} < 50$ s

[a]Required to be inside of the BP with the MWPC signal >200 channels.
[b]Required to be outside of the BP with its full energy in the ID and MWPC signals <200 channels.

by an α-like particle [as described in (i)] within the same pixel.

(iii) EVR-α-α correlations consisting of an EVR-α correlation [as described in (ii)] and followed within 108 s (three times the 36-s ^{248}Fm half-life) by an a-like particle [$7.7 < E_\alpha$ (MeV) < 7.95] within the same pixel.

(iv) EVR-SF correlations consisting of an EVR [$5.0 < E_{\rm EVR}$ (MeV) < 12.0, coincident with the BP and the MWPC] followed within 6.9 s by a SF-like event [$80 < E_{\rm SF}$ (MeV) < 300, $E_{\rm ID} < 200$ MeV, anticoincident with the BP and the MWPC] in the same pixel.

All events were required to be anticoincident with the punch-through detectors. All α and SF-like events were required to be anticoincident with the MWPC and to occur outside of the BP, where the background from low-ionizing particles was greatly reduced. α-like events also were required to have their full energy deposited in the ID because of the better energy resolution and lower background associated with those events.

^{253,254}No predominantly are longer-lived α-decaying isotopes (^{253}No: $t_{1/2} = 1.7$ min, $E_\alpha = 8.010$ MeV, ^{254}No: $t_{1/2} = 55$ s, $E_\alpha = 8.093$ MeV) with longer-lived α-decaying daughters (^{249}Fm: $t_{1/2} = 2.6$ min, $E_\alpha = 7.527$ MeV, ^{250}Fm: $t_{1/2} = 30$ min, $E_\alpha = 7.430$ MeV). Because of the rate of ^{253,254}No-like α particles [$7.85 < E_\alpha$ (MeV) < 8.25, anticoincident with the BP and the MPWC, full energy deposited in ID] and the rate of EVR-like events [$5.0 < E_{\rm EVR}$ (MeV) < 12.0, coincident with the BP and the MWPC], approximately one to three random EVR-like events are expected to be correlated to each ^{253,254}No-like α decay within three average half-lives of ^{253,254}No. As such, safely correlating a ^{253,254}No-like α particle to a nonrandom EVR was not possible. The amount of ^{253,254}No implanted in the FPD was determined based on the integral of ^{253,254}No-like α decays with their full energy deposited in the ID that occurred outside of the BP, where the background in the α-particle energy region was significantly lower.

Decay properties assigned to ^{288,289}114 as measured at the DGFRS have been previously published [23]. Guided by these results, we searched for time- and position-correlated decay chains, which consist of an EVR, one or more α-like events, and terminate with a SF. Element 114 EVRs were defined as events during the BP with $3.0 < E_{\rm EVR}$ (MeV) < 15.0, coincident with a signal from the MWPC and anticoincident with the punch-through detectors. α- and SF-like events were anticoincident with both the MWPC and the punch-through detectors. α-like events could occur either inside or outside BPs. For portions of the experiment, the terminating SF was required to occur outside of the BP.

^{288}114 was identified by detection of EVR-α-SF correlations that consisted of an EVR followed by an α particle [$9.7 < E_\alpha$ (MeV) < 10.2] within 7 s and a terminating SF within 1 s. ^{289}114 was identified by EVR-α-α-SF correlations that consisted of an EVR followed by an α particle [$9.7 < E_\alpha$ (MeV) < 10.2] within 7 s, a subsequent α particle [$9.0 < E_\alpha$ (MeV) < 9.5] within 150 s, and was terminated by SF within 50 s of the last α particle. We also searched for additional EVR- or α-like [$8.0 < E_\alpha$ (MeV) < 12.0] events between the EVR beginning the chain and the terminating SF. Direct SF of ^{288,289}114 was not searched for because of the high rate of SF-like events. A summary of all search conditions for $^{252-254}$No and ^{288,289}114 are contained in Table II.

III. RESULTS AND DISCUSSION

A. Characteristics of the detectors

The $^{206-208}$Pb(^{48}Ca,2n)$^{252-254}$No reactions were primarily used to check the transmission of TASCA, the energy

calibration of the FPD, and to derive proper selection criteria on signals from the electronics. In the presence of a beam, the FPD was calibrated by using reactions of ^{48}Ca with ^{206,208}Pb. The energy resolution was 25-keV FWHM for 8.1-MeV α particles that deposited their full energy in the ID. For α particles that deposited a fraction of that energy inside the ID and the remainder in the upstream detector, the FWHM for an 8.1-MeV α particle was 170 keV. This large FWHM is caused by the wide variety of angles with which the α particle can leave the ID and still implant in the upstream detector. As the upstream detectors are not position sensitive, the angle of escape was not accurately known, which made dead-layer corrections on an event-by-event basis impossible. The calibration of the upstream detectors was checked by using reconstructed α particles from the ^{208}Pb(^{48}Ca,2n)^{254}No reaction.

During the $^{206-208}$Pb irradiations, low-energy tailing of α lines of implanted nuclei formed in transfer reactions was noticed. Because of the comparatively long lifetimes of $^{252-254}$No and their daughters, corrections were not necessary to the α-particle energies during the 231.2-MeV irradiation. Throughout the 254.6- and 259.4-MeV irradiations of the ^{244}Pu targets, a wide variety of TRPs reached the TASCA FPD, besides the EVRs of interest. The half-lives of several of these products (^{220}Ra: $t_{1/2} = 18$ ms, $E_\alpha = 7686$ keV; ^{215}At: $t_{1/2} = 0.1$ ms, $E_\alpha = 8024$ keV; ^{219}Fr: $t_{1/2} = 20$ ms, $E_\alpha = 7312$ keV; ^{214g}Fr: $t_{1/2} = 5.0$ ms, $E_\alpha = 8427$ keV; ^{218}Rn: $t_{1/2} = 35$ ms, $E_\alpha = 7129$ keV; ^{216}Rn: $t_{1/2} = 45$ μs, $E_\alpha = 8050$ keV; ^{216}Po: $t_{1/2} = 0.145$ s, $E_\alpha = 6778$ keV; ^{214}Po: $t_{1/2} = 164$ μs, $E_\alpha = 7686$ keV) were sufficiently short that deviations in the energy of the α particles were noticeable. These deviations were found to be a function of the energy of the event in the same strip that preceded the α particle and the time difference between the α particle and its preceding event, as can be seen in Fig. 4. Sufficient data were available to apply corrections to low-energy events preceded by events with energies of (i) ~6–9 MeV where α-α correlations of TRPs could be analyzed and (ii) 40–60 MeV through recoil-α correlations as TRP recoils are formed with twice the momentum of the beam and implant into the detector with these energies. Corrected (right) and uncorrected (left) spectra are contained in Fig. 4 for α particles preceded by events with energies of 40–60 MeV (top) and 6–9 MeV (bottom). Where sufficient data existed, a correction of all low-energy (<15 MeV) events was made to account for these energy deviations. No energy correction was necessary for any event contained in the ^{288,289}114 chains.

The high-energy calibration used for measuring fission fragment energies was obtained from extrapolating the calibration from the α-energy region. This calibration was tentatively verified using SF events produced in the ^{206}Pb(^{48}Ca,2n)^{252}No reaction. However, insufficient data were obtained for a more accurate calibration. The high-energy calibration of the upstream detector was rather poor because of the lack of high-statistics calibration data.

During portions of the ^{244}Pu(^{48}Ca,3-4n) experiment (~67%), pinholes and/or rips in the targets allowed a fraction of the ^{48}Ca^{10+} beam to enter TASCA in the initial 10+ charge state without being stripped inside the target backing and target material. During the other 33% of the irradiation, where target

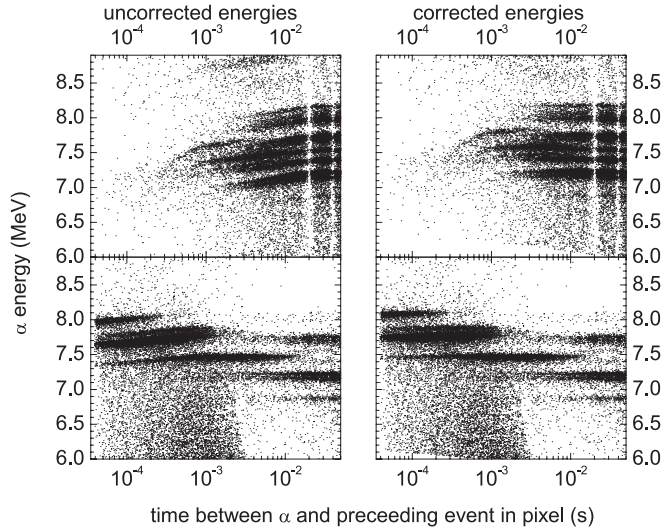

FIG. 4. (Left) Uncorrected and (right) corrected energies of α particles from transfer reactions that occurred in the same pixel and immediately followed (top) a high-energy EVR [40 < $E_{\rm EVR}$ (MeV) < 60] or (bottom) an α particle [6.0 < E_α (MeV) < 9.0] within 0.05 s. The time structure in the top graphs is a result of requiring α particles to occur outside of the BP.

integrity was not compromised, an estimated 100 ^{48}Ca beam particles per second left the target with a 10+ charge state. A fraction of this ^{48}Ca^{10+} (5%–10%) was then directed to the FPD by TASCA. Since the MWPC was only ~99% effective at distinguishing a ^{48}Ca^{10+} passing through, a portion of the beam approximated SF events. To differentiate between SF events and events originating from the ^{48}Ca beam, the ^{206}Pb(^{48}Ca,2n) reaction was used to produce ^{252}No ($t_{1/2} = 2.3$ s), which had a SF-branching ratio of 26.9% [35]. Spectra of MWPC signals for all high-energy [80 < E (MeV) < 250] events correlated within 10 s to EVR-like events [3 < $E_{\rm EVR}$ (MeV) < 15] during the ^{206}Pb(^{48}Ca,2n)^{252}No experiment are shown in Fig. 5. In correlations involving high-energy events that were outside of the BP, the recorded MWPC signal was peaked at ~150 channels and was extended out to ~200 channels. The time difference between the high-energy events and their associated recoils were plotted (see Fig. 5 inset), and a half-life of ~2.2 s for these correlations was observed, which indicated that they were caused by the SF decay of ^{252}No. When the high-energy event occurred inside of the BP, the MWPC signals peaked around 310 channels, with shoulders at ~250 and ~500 channels. A separate significantly smaller peak occurred between 100 and 200 channels. Further analysis of the events in the peak below 200 channels showed that they decayed with a lifetime of ~2.1 s, characteristic of ^{252}No (see Fig. 5 inset), while events in the peak at ~310 channels did not decay with a characteristic lifetime, which indicated that they were components of background. As such, the threshold for a valid MWPC signal was set at 200 channels. SF and α events were required to have MWPC signals below 200 channels, while EVRs were required to have signals above 200 channels.

While requiring SF events to be anticoincident with the MWPC significantly reduced the number of beam particles

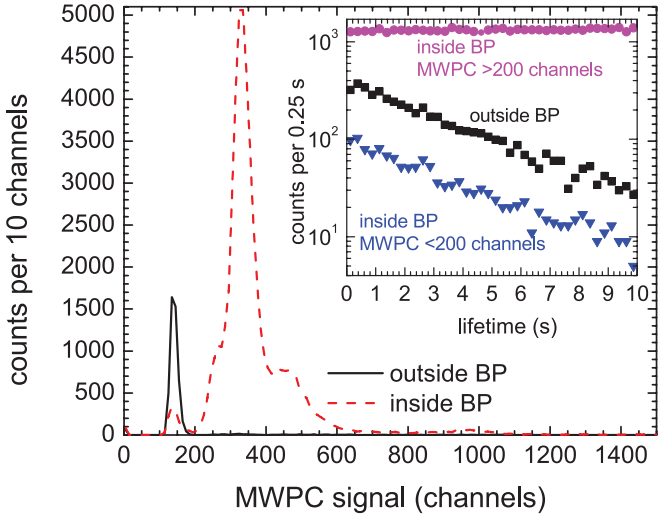

FIG. 5. (Color online) Spectra of MWPC data from correlations between EVR-like and high-energy [80 < E (MeV) < 250] events during the ^{206}Pb(^{48}Ca,2n)^{252}No experiment with the high-energy event occurring either (solid) outside or (dashed) inside the BP. The inset shows the time difference between each high-energy event and the associated EVR-like event for all correlations with the high-energy event occurring outside of the BP (●), and for all correlations with the high-energy event occurring inside the BP with MWPC signals either >200 channels (■) or <200 channels (▼).

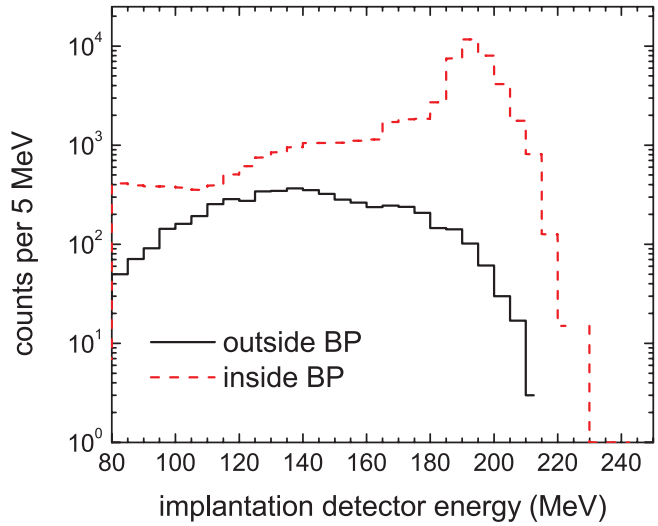

FIG. 6. (Color online) Energy spectra of all high-energy events from correlations between EVR and high-energy [80 < E (MeV) < 250] events during the ^{206}Pb(^{48}Ca,2n)^{252}No experiment when the high-energy event occurred either (solid line) outside or (dashed line) inside the BP.

approximating SF events, the distribution of the MWPC signal from beam particles entering the FPD is broad enough that a fraction of beam particles (∼1%) have MWPC signals <200 channels. To further distinguish beam and SF events, the energy distribution of the ID portion of high-energy events from correlations between EVRs and high-energy events in the ^{206}Pb(^{48}Ca,2n) reaction were analyzed, with the spectra shown in Fig. 6. For high-energy events that occurred inside the BP, and attributed in the previous paragraph to the ^{48}Ca beam that entered the FPD, a peak occurs at 190 MeV with a FWHM of 13 MeV and a significant low-energy tail. The high-energy events outside of the BP (attributed to ^{252}No) had a broad peak centered around 140 MeV. This energy difference was used to further distinguish SF events by requiring the energy in the ID E_{ID} to be <175 MeV if the SF event occurred inside of the BP, which reduced the detection efficiency of inside-the-BP SF events by 13%.

For the ^{244}Pu(^{48}Ca,3-4n) reactions, the energy of the ^{48}Ca beam was 25–30 MeV higher than that used in the ^{206}Pb(^{48}Ca,2n) reaction at the center of the target. After taking pulse-height defects into account, the peak from the scattered beam was expected to occur around 220 MeV in the ^{244}Pu(^{48}Ca,3-4n) reactions. Various theories [36,37] predict that the total kinetic energy (TKE) of the SF of ^{277}Hs, ^{281}Ds, and ^{284}Cn is ∼30 MeV higher than the TKE of ^{252}No, which indicates ID energies centered around 150 MeV. Because of this, SF events were defined as events with 80 < E_{SF} (MeV) < 400, E_{ID} (MeV) < 200 for all ^{244}Pu irradiations to maximize the efficiency for detecting SF decays while minimizing the contribution of random SF-like events from the ^{48}Ca beam. Even with this restricted definition of a SF-like event, the rate of SF-like events during the BP was 0.01–0.1 s^{-1} for 58% of the experiment, while an additional 5% and 4% of the experiment had rates of 0.1–1 and >1 s^{-1}, respectively. As such, for portions of the run where background from the ^{48}Ca beam approximated SF-like events with a rate higher than 0.01 s^{-1} (67% of the experiment), SF events were required to occur outside of the BP to reduce contributions from the low-energy tailing of the beam peak.

B. EVR image in TASCA

The ^{48}Ca beam entered the targets with a beam size of 6-mm diameter. Because of the momentum of the beam, EVRs are formed with a forward focus, although they experience scattering in the target. The large number of reaction products from the ^{48}Ca + ^{206}Pb reactions allowed for a quantification of the effect of scattering in the 558-μg cm^{-2} ^{206}PbS target and of the magnification of the EVR image in TASCA. Figure 7 shows the position of ^{252}No decays at a magnetic rigidity setting of 2.10 T m along with the distribution predicted by the Monte Carlo simulation of EVR trajectories (as described in Sec. II A) in the HTM of TASCA. The experimental focal-plane image had a FHWM of 58 mm in the horizontal direction and 22 mm in the vertical direction. This is slightly larger than that predicted by the simulations, likely caused by scattering of the EVRs in the MWPC, which was not included in the simulation, but could indicate over- or underfocusing of the quadrupoles. For the SIM, the predicted and experimental positions of ^{254}No decays are shown in Fig. 8. The simulation accurately predicts the distribution of ^{254}No decays, although insufficient data were available to determine position distributions for SIM.

During the experiment, the $B\rho$ of TASCA was changed to move the implantation ^{252}No events to the edges of the ID. This allowed for measuring the dispersion in TASCA [mm/(% change in $B\rho$)]. It was determined to be 6.5 mm/(% $B\rho$).

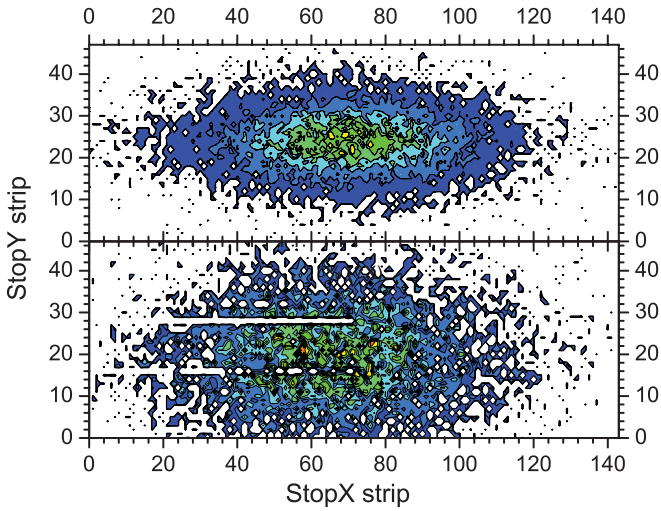

FIG. 7. (Color online) (Top) Simulated and (bottom) experimental distribution ^{252}No decays for the HTM of TASCA. StopY strips 16 and 28 were not working properly, as indicated by the lack of counts.

This is slightly smaller than the 8 ± 1 mm/(% $B\rho$) dispersion predicted by the TASCA simulations as described in Sec. II A.

At a TASCA $B\rho$ setting of 2.10 T m, the $^{252-254}$No EVRs were centered at strip 66.4 ± 0.3. Based on the measured TASCA dispersion, this indicates that the $^{252-254}$No EVR $B\rho$ is (2.084 ± 0.011) T m. This is comparable to the ^{254}No $B\rho$ of 2.085 T m that was measured at the BGS with a helium pressure of 67 Pa, although slightly higher than the $B\rho$ of 2.04 T m that was measured at GARIS [38].

C. The $^{206-208}$Pb(^{48}Ca,2n) $^{252-254}$No reactions

1. ^{252}No decay properties

The half-life measured for ^{252}No based on ∼8000 EVR-α and EVR-SF correlations was (2.47 ± 0.02) s, in agreement with, but more precise than, literature values of $2.38^{+0.26}_{-0.22}$ s [15], (2.44 ± 0.04) s [6], (2.30 ± 0.22) s [39], (2.44 ± 0.12) s [40], and (2.42 ± 0.06) s [13]. The SF-branching ratio was calculated to be (29.3 ± 0.9)%, which is comparable to literature values of (32 ± 3)% [15], (32.2 ± 0.5)% [6], and (26.9 ± 1.9)% [39], although slightly larger than the value of (21.6 ± 4.2)% from Andreyev *et al.* [41]. For ^{248}Fm, analysis of ∼1000 EVR-α-α correlations yielded a half-life of (35.1 ± 0.8) s, which is in good agreement with, but more precise than, the previously measured value of (36 ± 3) s [35].

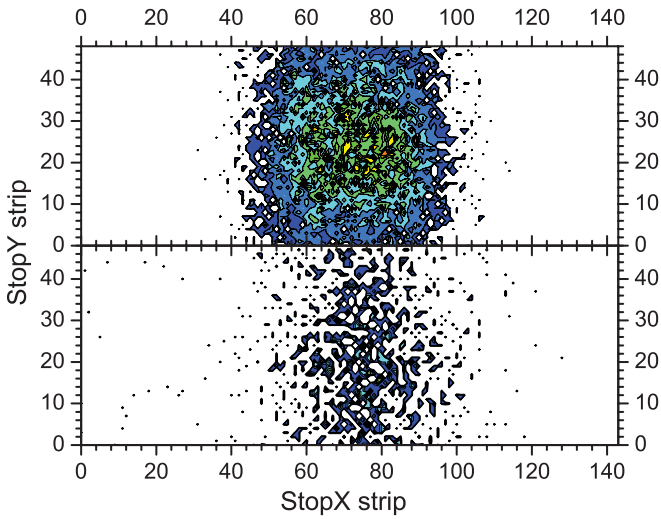

FIG. 8. (Color online) (Top) Simulated and (bottom) experimental distribution ^{254}No decays for the SIM of TASCA.

2. Cross sections

To examine TASCA's ability to accurately determine cross sections, excitation functions measured at the BGS [8], the DGFRS [6], the SHIP [12–14], and the VASSILISSA [15] were compared. To avoid discrepancies arising from comparing the TASCA data to measurements at single points rather than at the maximum of the excitation function, fits were performed on the data from each of the separators, employing a Gaussian on the low-energy side smoothly joined to an exponential tail on the high-energy side,

$$\sigma = Ae^{-(E-c)^2/2w^2}, \quad E \leqslant \lambda w^2 + c, \tag{1}$$

$$\sigma = Ae^{\lambda^2 w^2/2} e^{-\lambda(E-c)}, \quad E > \lambda w^2 + c, \tag{2}$$

where σ is the cross section as a function of the ^{48}Ca beam energy E, A is the amplitude at the centroid c, of a Gaussian with width w, and λ is the exponential slope.

For the $^{206-208}$Pb(^{48}Ca,2n)$^{252-254}$No excitation functions, both global and best fits were performed to determine the influence of varying λ and w on the maximum cross section. Before fitting, systematic errors were removed from the data, as these errors are constant for a given reaction and separator. For the global fit, λ and w values were fixed at 0.34 MeV^{-1} and 2.9 MeV, respectively, allowing only c and σ to vary until the solution converged. In the best fit, all values were allowed to vary until the solution converged if sufficient data were available to fit the shape of the excitation function. The λ, w, c, and maximum σ values for all data are contained in Table III. For TASCA, c was fixed at the c of the SHIP, under the assumption that differences in the energy at the peak of the excitation are caused by systematic uncertainty energies from individual accelerators. In all cases, differences between the cross sections at the maximum of the excitation function according to the global and best fits differed by less than 6% ($\leqslant$3% in 9 of 11 cases), indicating that the maximum cross section is stable over a range of ±10% for λ and w.

The ^{208}Pb(^{48}Ca,2n)^{254}No excitation functions and their global fits at the BGS [8], DGFRS [6], SHIP [12,14,42], and VASSILISSA [15] data are shown in Fig. 9. The resulting cross sections at the maximum of the excitation functions were as follows: (2250 ± 350), (2370±180), (1760 ± 60), and (1920 ± 260) nb for the BGS, DGFRS, SHIP, and VASSILISSA, respectively. The cross-sectional values for the two gas-filled separators (BGS and DGFRS) agree well. A similar agreement is observed in the cross-sectional estimate for the two velocity filters (SHIP and VASSILISSA), however, the velocity filters measure a cross section that is ∼22% lower than that measured at the gas-filled separators. This

TABLE III. Fitting parameters and maximum cross sections from the fit for experimental data.

Reaction	Separator	Global fit σ_{max} (nb)[a]	Best fit[b]				References
			λ (MeV^{-1})	c (MeV)	w (MeV)	σ_{max} (nb)[c]	
^{208}Pb(^{48}Ca,2n)^{254}No	BGS	2250 ± 380	0.35	216	2.6	2270 ± 190	[8]
	DGFRS	2370 ± 180	0.34	216	**3.1**	2300 ± 120	[6]
	TASCA	2100 ± 140	**0.31**	**216**	**2.8**	2030 ± 170	This paper
	SHIP	1760 ± 60	0.31	216	2.8	1800 ± 80	[12,14]
	VASSILISSA	1920 ± 260	0.34	217	3.1	1810 ± 440	[15]
^{207}Pb(^{48}Ca,2n)^{253}No	DGFRS	1130 ± 170	**0.34**	217	**2.6**	1190 ± 130[d]	[6]
	TASCA	870 ± 10	**0.31**	**216**	**2.8**	880 ± 10	This paper
^{206}Pb(^{48}Ca,2n)^{252}No	DGFRS	500 ± 40	0.34	217	2.6	500 ± 40	[6]
	TASCA	350 ± 10	**0.31**	**216**	**2.8**	350 ± 10	This paper
	SHIP	430 ± 10	**0.31**	216	**2.8**	430 ± 10	[13]
	VASSILISSA	320 ± 30	0.34	217	2.9	320 ± 80	[15]

[a]Maximum cross sections as a result of a fit for experimental data with $\lambda = 0.34$ MeV^{-1}, $w = 2.9$ MeV. c and σ were allowed to vary.
[b]Numbers in bold were fixed for the fit, all other numbers were allowed to vary.
[c]Errors do not include systematic uncertainties.
[d]Increasing w to 3.1 MeV resulted in a similar $\sigma_{max} = (1110 \pm 190)$ nb.

difference may indicate systematic over- or underestimates of transmission efficiencies through the different types of separators or the presence of a short-lived (>100 ns, <1 μs) isomer in ^{254}No. The decay of this isomer would change the ^{254}No charge state, reducing the transmission efficiency in the velocity filters but not in the gas-filled separators.

For TASCA, the cross sections for the ^{208}Pb(^{48}Ca,2n) reaction were measured to be (1890 ± 40) nb in the 231.2-MeV HTM irradiation and (1650 ± 40) nb in the 231.2-MeV SIM irradiation, after correcting for the α-branching ratio. The lower cross section in the 231.2-MeV SIM irradiation (which was performed after the 231.2-MeV HTM irradiation) indicates that some of the ^{208}PbS target material was lost because of sputtering or evaporation during the two experiments. A fit at the 231.2-MeV HTM irradiation, assuming the SHIP λ, w, and c values, indicates that the maximum cross section is 2100 ± 140 nb. This value is lower than (although within 1σ of) the cross sections measured at the other gas-filled separators. However, this is to be expected if an unknown amount of target material was sputtered or was evaporated off the target during the irradiation.

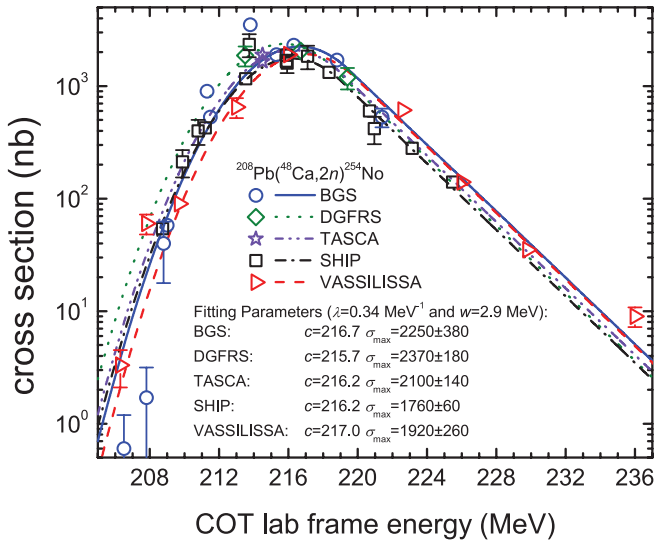

FIG. 9. (Color online) ^{208}Pb(^{48}Ca,2n)^{254}No excitation functions measured at the BGS (○), the TASCA(☆), the DGFRS (◇), the SHIP (□), and the VASSILISSA (△). Error bars are shown when larger than the points and represent statistical errors only. The lines are fits for the excitation functions as described in Sec. III C2, with $\lambda = 0.34$ MeV^{-1} and $w = 2.9$ MeV. c and σ were allowed to vary and converged to the values shown in the figure.

A cross section of 760 ± 10 nb was measured for the ^{207}Pb(^{48}Ca,2n) reaction by using TASCA in the HTM. Excitation function measurements are also available for the DGFRS [6]. These data suggest that the maximum cross sections are (1130 ± 170) and (870 ± 10) nb at the DGFRS and TASCA, respectively. The fit for the DGFRS value is ~23% higher than the TASCA value, consistent with what was observed in the ^{208}Pb(^{48}Ca,2n) reaction and with the prior assumption of loss of target material during irradiation.

For the ^{206}Pb(^{48}Ca,2n) reaction, experimental data were available for the DGFRS [6], the SHIP [13], and the VASSILISSA [15]. A cross section of (310 ± 10) nb was measured during the 231.2-MeV irradiation at TASCA. The resulting cross sections at the maximum of the excitation function were (500 ± 40), (350 ± 10), (430 ± 10), and (320 ± 30) for the DGFRS, the TASCA, the SHIP, and the VASSILISSA, respectively. The maximum cross section from the TASCA experiment is in agreement with the VASSILISSA data but is 19%–30% lower than the cross sections from the DGFRS or the SHIP. Again, this is an indication that target material is being lost during the irradiation.

Between the four separators, the maximum cross sections varied by 25%–50% for the $^{206-208}$Pb(^{48}Ca,2n) reactions. The large deviation between measurements at individual separators indicates that there are difficulties in accurately measuring cross sections at or below the microbarn level.

D. α-γ coincidences

The ^{207}Pb targets were used to produce ^{253}No to cross-check the γ-ray energy calibration and the timing correlation of the germanium cluster detector with the event trigger. During this test, $\sim$1200 ^{253}No α particles [$7.9 < E_\alpha$ (MeV) < 8.3, anticoincident with MWPC] were observed. Two γ-ray peaks at 222.2 and 279.2 keV were readily observed, in agreement with the data from Ref. [16]. Nevertheless, a timely off-line check of the ^{253}No data proved that the yield of these peaks in relation to the number of detected ^{253}No α particles was too low given the expected detection efficiency of the cluster of some 15%–20% at these γ-ray energies. This was corrected early on in the element 114 production run by changing a delay constant in the sampling ADC and cross-checked with α-γ coincidences arising from a standard ^{241}Am source.

E. The ^{244}Pu(^{48}Ca,3-4n)^{288,289}114 reactions

1. ^{288}114

Eleven EVR-α-SF chains observed in the ^{48}Ca + ^{244}Pu reaction were assigned to the decay of ^{288}114 (events 2–8, 10, 11, and 14, 15 in Table IV). Eight of these events were observed during the 259.4-MeV HTM irradiation, and one additional event was observed during the 254.6-MeV HTM irradiation. These were previously published in Ref. [26]. Two additional events were observed during the 259.4-MeV SIM irradiation. The half-life that originates from these 11 decays is $0.52^{+0.22}_{-0.13}$ s for ^{288}114 and $0.11^{+0.05}_{-0.03}$ s for ^{284}Cn, in agreement with those published in Ref. [23]. The α-particle energy from the eight ^{288}114 decays in which the full α-particle energy was deposited in the ID is (9.95 ± 0.03) MeV, in agreement with the (9.94 ± 0.06) MeV observed in Ref. [23].

Two of the eleven observed ^{288}114 decay chains were recorded while TASCA was operated in the SIM. The observation of two chains is consistent with the reduced efficiency and beam dose. These results indicate that, even with the reduced transmission, using TASCA in the SIM to study the chemistry of element 114 is feasible.

2. ^{289}114

Four EVR-α-α-(α)-SF chains were observed during the HTM portion of the ^{48}Ca + ^{244}Pu irradiation, two each at 259.4 and 254.6 MeV (events 1, 9, 12, and 13 in Table IV). Half-lives of $0.97^{+0.97}_{-0.32}$, 30^{+30}_{-10}, and 20^{+20}_{-7} s were observed for ^{289}114, ^{285}Cn, and ^{281}Ds, respectively. The half-life of ^{285}Cn is in agreement with that published in Ref. [23], and those for ^{289}114 and ^{281}Ds agree within 2σ. All four ^{289}114 and ^{285}Cn decays resulted in the full energy of the α particle being deposited in the ID. Based on these decays, the α-particle energies of ^{289}114 and ^{285}Cn are (9.87 ± 0.03) and (9.21 ± 0.03) MeV, respectively. These are slightly higher than, but still in agreement with, the α-particle energies observed in Ref. [23] of (9.82 ± 0.05) and (9.15 ± 0.05) MeV for ^{289}114 and ^{285}Cn, respectively.

Chain 1 from Table IV differs from all chains published in Ref. [23]. ^{281}Ds was previously observed to decay only by SF [20,43]. We observed an EVR-α-α-SF chain consistent with the decay of ^{289}114. However, between the second α particle and the SF decay, we observed an (8.727 ± 0.025)-MeV α particle with a lifetime of 5.688 s, followed 4.502 ms later by the terminating SF, resulting in an EVR-α-α-α-SF correlation. While the energy region around 8.685 MeV is near α lines of background activities, such as ^{211m,212}Po, a statistical analysis indicates that there is only a 0.1% probability that this α particle is unrelated to the other members of the decay chain. We assigned this event to the α decay of ^{281}Ds [26], followed by SF of the new isotope ^{277}Hs, a previously unknown nucleus with $Z = 108$, which has been shown to be a deformed proton shell closure in lighter isotopes with $N \sim 162$ [44].

The observed lifetime of ^{277}Hs results in a half-life of 3^{+15}_{-2} ms, which is short compared to half-lives of lighter Hs isotopes, which are situated near the deformed neutron shell closure at $N = 162$. Furthermore, these Hs isotopes have only been observed to undergo α decay, with a conservative lower limit of $t_{1/2}$ (SF) on the order of 10 s [44,45]. However, the short measured lifetime for ^{277}Hs is in good agreement with theoretical predictions for Hs isotopes based on the macroscopic-microscopic model [46], which lists 46 ms (^{276}Hs) and 0.98 ms (^{278}Hs) for the neighboring even isotopes (odd isotopes were not calculated). The geometric mean of the predicted half-lives of the neighboring $^{276-278}$Hs is 6.7 ms. The odd neutron in ^{277}Hs is expected to hinder SF decay by several orders of magnitude. A comparison of experimental [23] and theoretical [47] values for even-even copernicium isotopes, where more experimental data are available for such a comparison, suggests that theory overestimates partial SF half-lives near $N \sim 170$ by 1 to 2 orders of magnitude, which, thus, seems to be the accuracy of these calculations. By respecting the huge variations of $t_{1/2}$ (SF) with N—in the case of Hs isotopes with N between 152 and 184, the predicted [46,47] $t_{1/2}$ (SF) cover 17 orders of magnitude—and the accuracy of such predictions, the agreement between the geometric mean of the predicted half-lives of the neighboring $^{276-278}$Hs (6.7 ms) and our measured lifetime (4.5 ms) is good.

Theory suggests that nuclei with $N \sim 170$ are located in a region of minimum shell stabilization between the deformed neutron shell closure $N = 162$ and the expected spherical shell closure at $N = 184$ [48]. Only limited $t_{1/2}$ (SF) data for this region are available, and so far, none for elements where isotopes with $N \sim 162$ are known. Our data point for ^{277}Hs continues the Hs isotopic chain, which covers the $N = 162$ shell closure region well, toward more neutron-rich isotopes, see Fig. 10. It verifies the influence of this shell on $t_{1/2}$ (SF). So far, SF has not been observed for any Hs with $N > 156$, including the recently observed ^{273}Hs [25]. Its reappearance at $N = 169$ demonstrates that stability toward SF caused by the influence of this shell vanishes with increasing distance from $N = 162$, at least until the $N = 170$ region.

3. Coincident x and γ rays

Detection of characteristic x rays following α decay of any of the events in the 114 chains would allow for a direct

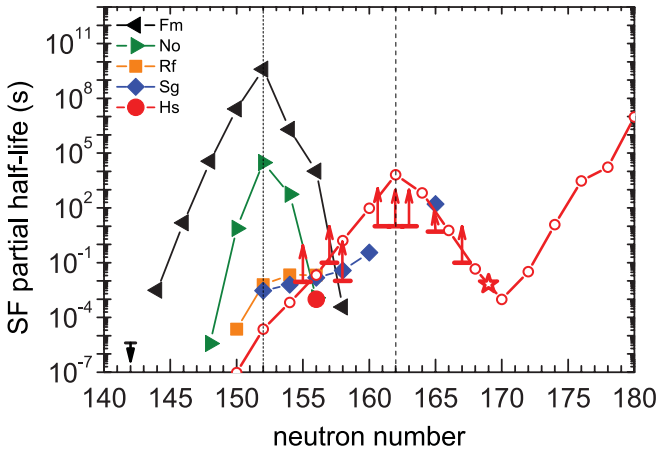

FIG. 10. (Color online) Systematics of spontaneous fission partial half-lives vs neutron number. Solid symbols show experimental data. (Dashed lines) Locations of deformed shell closures at $N = 152$,162. Experimental data for Fm and No isotopes highlight the influence of the $N = 152$ shell closure (solid triangles). The hassium isotopic chain covers the region around the $N = 162$ shell. Open circles show calculated values for even Hs isotopes [46]. The experimental point for ^{264}Hs is shown by the solid circle. Experimental lower limits are shown with arrows. Our data point for ^{277}Hs is shown by the open star. The experimental [23,44,45,49–54] Hs isotopic chain pattern shows that the influence of the $N = 162$ shell vanishes as the minimum between the island of deformed superheavy nuclei centered at ^{270}Hs, and the predicted island of spherical superheavy nuclei near $N = 184$ is approached.

determination of the atomic number of the decay product. During the ^{48}Ca + ^{244}Pu irradiation, we searched for x and γ rays in coincidence with any decay in the ^{288,289}114 decay chains, with the exception of chain 1 in Table IV, where the detection of γ-ray coincidences was not yet working properly (see Sec. III D). Prompt γ rays were detected in coincidence with the SF events in 11 of the remaining 14 chains (chains 3, and 6–15 in Table IV). Of those 11 SF events, 8 had one γ ray each, while the remaining 3 SF events were correlated with two γ rays each when add back of neighboring germanium crystals was enforced. No x or γ rays were observed in prompt coincidence with any EVR implant or α particle from the ^{288,289}114 decay chains.

4. Cross sections

The ^{244}Pu(^{48}Ca,xn) reaction was investigated at excitation energies of $E^* = 36.1$–39.5 and $E^* = 39.8$–43.9 MeV. Cross sections at $E^* = 36.1$–39.5 were measured to be $8.0^{+7.4}_{-4.5}$ pb for the $3n$ exit channel and $2.8^{+4.2}_{-2.1}$ pb for the $4n$ exit channel [26]. At $E^* = 39.8$–43.9 MeV, cross sections were measured to be $3.5^{+3.3}_{-2.0}$ and $9.8^{+3.9}_{-3.1}$ pb for the $3n$ and $4n$ exit channels, respectively. Error bars include statistical uncertainties at the 68.3% confidence level and are calculated according to Ref. [55]. Figure 11 shows cross sections for the $3n$ and $4n$ exit channels of the ^{244}Pu(^{48}Ca,xn) reaction for this paper along with the excitation function predictions from Ref. [22]. Horizontal error bars represent the range of beam energies covered inside the target,

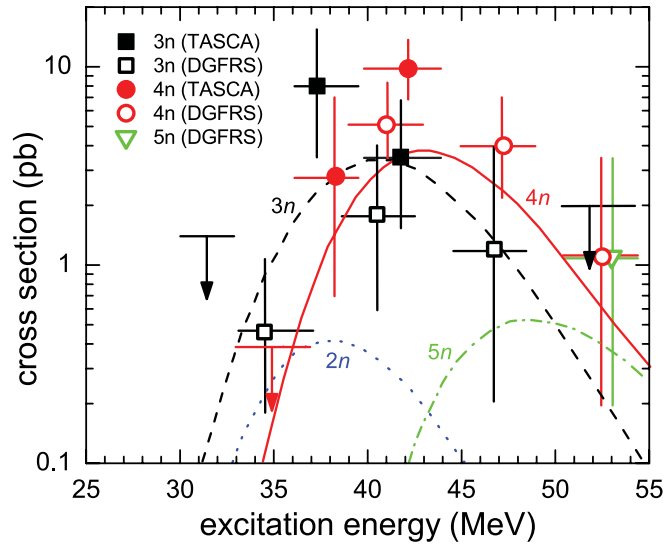

FIG. 11. (Color online) Cross sections for the ^{244}Pu(^{48}Ca,3-4n) reaction as observed in this paper (solid symbols) and from Ref. [23] (open symbols). Lines are cross-sectional predictions for the 2, 3, 4, and 5n exit channels from Ref. [22].

while vertical error bars represent the uncertainties caused by counting statistics and are presented at the 1σ level. Also included in Fig. 11 are the 3 to 4n cross sections observed at the DGFRS [18]. At $E^* = 39.8$–43.9 MeV, cross sections from this paper are higher than those from $E^* = 38.9$–43.0 in Ref. [18], although they agree within 1σ. In addition, at $E^* = 36.1$–39.5 MeV, we observe a $3n$ cross section that is four times the $3n$ cross section reported in Ref. [18], although they also agree within 1σ. This large difference may be due, in part, to the difference in irradiation energies used in this paper and in Ref. [18] or the difficulties in accurately measuring small cross sections as discussed in Sec. III C2.

5. Magnetic rigidity

The $B\rho$ of element 114 EVRs in 80-Pa He was measured to be (2.29 ± 0.11) T m in the 259.4-MeV HTM run, where the best statistics were obtained, based on the observed horizontal position of the element 114 events in the ID and the assumed TASCA $B\rho$ of 2.23 T m. With the lower statistics in the 254.6-MeV HTM run, the $B\rho$ of element 114 EVRs in 0.8-mbar He was measured to be (2.29 ± 0.15) T m.

6. Background contributions

Figure 12 shows the total low [$7 \leqslant E$ (MeV) $\leqslant 12$] and high [$25 \leqslant E$ (MeV) $\leqslant 250$] energy spectra recorded in the ID during the HTM and SIM portions of the ^{48}Ca + ^{244}Pu run with a total accumulated beam dose of 4.59×10^{18}. The spectra of α- and SF-like events (as defined in Secs. III E1 and III E2) in the ID, both during and outside of the BP for the SIM and HTM runs, are also included. Energies of α and SF events within decay chains presented in Table IV are indicated. In the HTM high-energy spectra [Fig. 10)], a peak, caused by the scattered beam reaching the ID, appears at ∼225 MeV. The peak at ∼50 MeV in both the HTM and the SIM high-energy

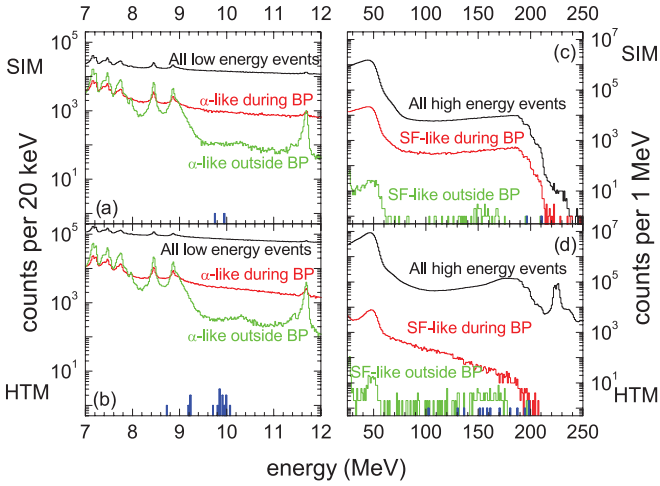

FIG. 12. (Color online) Energy spectra recorded in the ID during the 259.4-MeV HTM irradiation. (Left) Total energy spectra of all low-energy events and α-like signals during the BP and outside of the BP for the (a) SIM and (b) HTM portions of the run. (Right) Total energy spectra of all high-energy events and SF-like signals during and outside of the BP for the (c) SIM and (d) HTM portions of the run. The solid histograms show the energies of the α events [in (b)] and ID portion of energies of the SF events [in (d)] observed in correlated decay chains.

spectra is caused by the fraction of recoils from TRPs that are formed with twice the momentum of the beam, recoil out of the target, and are guided to the FPD by TASCA. A small portion of EVRs from TRPs appear to occur outside of the BP, a problem that was not remedied off-line (as discussed in Sec. III B). An additional peak occurs around 150 MeV in the SF-like events anticoincident with the BP. These events are correlated with high-energy recoils [$40 < E_{\text{recoil}}$ (MeV) < 60] on the millisecond (<20 ms) time scale and were assigned to the decay of americium fission isomers produced in transfer reactions.

Low-energy spectra for both HTM and SIM are dominated primarily by the α decay of short-lived products from transfer reactions having $Z_{\text{product}} < Z_{\text{target}}$. Cross sections for the production of below-target TRPs have been published for the ^{48}Ca + ^{248}Cm [56] and ^{48}Ca + ^{238}U reactions [51,52]. To determine suppression factors (the ratio of the predicted number of TRPs produced in the target to the observed number of TRPs in the FPD) for both modes of TASCA, the expected direct production yields of ^{218}Rn, ^{219}Fr, ^{220}Ra, and ^{212m}Po were estimated based on published data from Refs. [56–58]. The amount of ^{218}Rn, ^{219}Fr, and ^{220}Ra in the ID was estimated based on EVR-α-α correlations. For ^{212m}Po, the amount implanted into the ID was estimated based on the number of counts in the 11.65-MeV α-particle peak above the background. In all cases, α particles were required to deposit their full energy in the ID. The total number of ^{218}Rn, ^{219}Fr, ^{220}Ra, and ^{212m}Po in the ID were corrected for efficiency of α-particle detection, α-branching ratio, intensity of the α line, dead time of the detector between events, and the number of half-lives that correlations were searched out for. In HTM, unwanted below-target TRPs are suppressed by a factor of ∼700. In SIM, the suppression factor is increased to ∼2000.

7. *Random rates*

The number of expected random EVR-α-SF and EVR-α-α-SF correlations was calculated by taking the observed number of SF events and multiplying by the probability of observing an EVR-α or EVR-α-α correlation in the same pixel preceding the SF within the predefined time window. The rate of EVR-, α-, and SF-like events during and outside of the BP during normal operations is shown in Table V. During the portions of the run with a large number of pinholes in one of the three target segments, the rate of α-like events increased by a factor of 10. The rate of SF-like events inside the BP increased to 0.01–0.1 s^{-1} for 58% of the experiment, while an additional 5% and 4% of the experiment had rates of 0.1–1 and >1 s^{-1}, respectively. However, outside of the BP, the rate of SF-like events did not increase. As such, for portions of the run when the rate of SF-like events in the BP was >0.01 s^{-1}, SF-like events were required to occur outside of the BP.

During the experiment, there were 426 SF-like events that occurred outside of the BP. With the caveat that SF events occurred out of the BP, it was possible to widen the correlation search gates for ^{288,289}114. For ^{288}114, correlation gates were widened to EVR [$3.0 < E_{\text{EVR}}$ (MeV) < 15.0] followed by an α particle [$8.0 < E_{\alpha}$ (MeV) < 12.0] within 30 s and terminated by a SF-like event outside of the BP and within 50 s of the α particle. With these wide gates, we expected to observe 3.0 random correlations of unrelated events. A total of 15 chains were observed. Ten had decay properties similar to ^{288}114 and, thus, were assigned (see chains 2, 3, 5–8, 10, 11, 14, and 15 in Table IV). The remaining five chains were assigned to random correlations of unrelated events as a result of one or more of the following conditions: (i) the α energy was more than 500 keV lower than energies from the DGFRS experiments, (ii) the lifetime of the parent α was more than three times the longest ^{288}114 lifetime from the DGFRS experiments, or (iii) the lifetime of the fission event was more than three times the longest ^{284}Cn lifetime from the DGFRS experiments.

For ^{289}114, we searched for EVR-α-α-SF correlations that consisted of an EVR [$3.0 < E_{\text{EVR}}$ (MeV) < 15.0] followed by an α particle [$8.0 < E_{\alpha}$ (MeV) < 12.0] within 30 s, a second α particle [$8.0 < E_{\alpha}$ (MeV) < 12.0] within 150 s, and terminated by a SF-like event outside of the BP and within 50 s of the last α particle. A total of five EVR-α-α-SF correlations were observed where 1.3 were expected due to random correlations of unrelated events. Four of the EVR-α-α-SF correlations had decay properties similar to those published for ^{289}114 and, thus, were assigned (chains 1, 9, 12, and 13 in Table IV). The remaining correlation [EVR ($E_{\text{EVR}} = 8.88$ MeV)—α particle ($E_{\alpha} = 11.89$ MeV, $\tau_{\alpha} = 13.227$ s)–α particle ($E_{\alpha} = 8.81$ MeV, $\tau_{\alpha} = 109.602$ s)—SF (165 MeV, $\tau_{\text{SF}} = 6.05$ s)] was assigned to random uncorrelated decays of TRPs because of their α-particle energies.

Based on the decay properties of chains ending with out-of-beam SF events, we narrowed the gates to search for chains ending with in-beam SF events. During the portions of the run considered low background enough to extend this search, there were 15 499 SF-like events. ^{288}114 was identified by detection of EVR-α-SF correlations that consisted of an EVR followed by an α particle [$9.7 < E_{\alpha}$ (MeV) < 10.2] within

TABLE IV. Observed 114 decay chains in chronological order. For reconstructed energies, the energies recorded in the FPD and upstream detectors, respectively, are listed in parentheses. SF energies are shown in boldface.

E^* (MeV)	E_{beam} (MeV)	Chain number	TASCA mode	StopX strip	StopY strip	E_{EVR} (MeV)	Decay energy (MeV)	Lifetime	^{A}Z	Prompt γ rays[c]
41.7	259.4	1	HTM	22	11	6.41	9.847	3.589 s	$^{289}114$ [a]	
							9.212	22.147 s	^{285}Cn [a]	
							8.727		^{281}Ds [a]	
							211 (136 + 75)	5.688 s	^{277}Hs [a]	
								4.502 ms		
41.7	259.4	2	HTM	91	18	6.51	9.982	0.242 s	$^{288}114$	0
							196(187 + 9)	0.130 s	^{284}Cn [a]	0
41.7	259.4	3	HTM	103	31	7.60	9.814 (1.236 + 8.578)	1.348 s	$^{288}114$ [a]	0
							272 (130 + 142)	0.059 s	^{284}Cn [a]	1
41.7	259.4	4	HTM	83	18	5.97	10.062 (0.575 + 9.487)	0.649 s	$^{288}114$ [a]	0
							163 (151 + 12)	0.171 s	^{284}Cn	0
41.7	259.4	5	HTM	102	24	8.69	9.915	0.446 s	$^{288}114$ [a]	0
							194	0.087 s	^{284}Cn [a]	0
41.7	259.4	6	HTM	110	19 + 20 [b]	7.99	9.919	1.164 s	$^{288}114$	0
							222 (158 + 64)	0.343 s	^{284}Cn [a]	1
41.7	259.4	7	HTM	119	29	9.10	9.980	0.242 s	$^{288}114$ [a]	0
							180	0.026 s	^{284}Cn[a]	2
41.7	259.4	8	HTM	19	21 + 22 [b]	13.22	9.947	0.763 s	$^{288}114$	0
							198	0.029 s	^{284}Cn [a]	1
41.7	259.4	9	HTM	86	20 + 21 [b]	6.56	9.917	0.345 s	$^{289}114$ [a]	0
							9.194	51.037 s	^{285}Cn [a]	0
							198	35.476 s	^{281}Ds [a]	1
41.7	259.4	10	HTM	131	26	7.35	9.700 (0.838 + 8.862)	0.823 s	$^{288}114$ [a]	0
							170	0.063 s	^{284}Cn [a]	1
37.5	254.6	11	HTM	89	24	8.67	9.965	0.482 s	$^{288}114$ [a]	0
							161	0.401 s	^{284}Cn [a]	1
37.5	254.6	12	HTM	100	5	6.93	9.847	0.774 s	$^{289}114$ [a]	0
							9.229	9.542 s	^{285}Cn [a]	0
							278 (154 + 124)	28.413s	^{281}Ds [a]	2
37.5	254.6	13	HTM	122	40	3.26	9.847	0.904 s	$^{289}114$	0
							9.220	92.202 s	^{285}Cn [a]	0
							146 (102 + 44)	46.283 s	^{281}Ds [a]	1 [d]
41.7	259.4	14	SIM	59	47	8.458	9947	1.132 s	$^{288}114$ [a]	0
							210	0.043 s	^{284}Cn [a]	2 [d]
41.7	259.4	15	SIM	89	0	7.605	9848	0.921 s	$^{288}114$	0
							196	0.390 s	^{284}Cn [a]	1

[a]Decay observed outside of BPs.
[b]All events in chain were split between two StopY strips.
[c]Number of prompt γ rays observed with each event. The detection of prompt γ rays was not working for chain 1 (see Sec. III D).
[d]Includes an add-back event of neighboring germanium crystals.

7 s and a SF within 1 s. $^{289}114$ was identified by EVR-α-α-SF correlations that consisted of an EVR followed by an α particle [$9.7 < E_\alpha$ (MeV) < 10.2] within 7 s, a second α particle [$9.0 < E_\alpha$ (MeV) < 9.5] within 150 s, and terminated by a SF-like event within 50 s of the last α particle. Based on the number of correlations with out-of-beam SF events and the portion of the experiment during which in-beam SF could be correlated to, an additional 1.2 events were expected. One additional EVR-α-SF correlation was observed with an in-beam SF and narrow α-energy gates (chain 4 in Table IV).

The number of expected random decay chains using the narrowed α-energy gates and with the terminating SF outside of the BP was 4×10^{-4} and 2×10^{-4} for $^{288}114$ and $^{289}114$, respectively. When including in-beam SF events, the number of expected random correlations with the narrowed α-particle energy gates increased to 0.02 and 0.05 for $^{288}114$ and $^{289}114$, respectively. Thus, it is unlikely that any of the 15 assigned chains are the result of random correlations of unrelated events.

For each chain, all events between the EVR and the terminating SF were checked for additional EVR- or α-like [$8.0 < E_\alpha$ (MeV) < 12.0] events. Chain 1 in Table IV contained an additional EVR between α particles 1 and 2, in the same pixel as the decay chain. In addition to the extra EVR in chain 1, chain 13 also contains a 14.04-MeV EVR 124.336 s

TABLE V. Average rate of events over the ID during the HTM and SIM runs when target integrity was not compromised. The dc rate of events can be found by 0.25∗ (during BP) + 0.75∗ (outside of BP).

Target	Event type	During BP		Outside of BP	
		HTM (s^{-1})	SIM (s^{-1})	HTM (s^{-1})	SIM (s^{-1})
^{206}Pb	EVR: $3.0 < E_{EVR}$ (MeV) < 15.0	120			
	α: $8.25 < E_\alpha$ (MeV) < 8.55	0.37		0.12	
	α: $7.7 < E_\alpha$ (MeV) < 7.95	0.33		0.09	
	α: $8.0 < E_\alpha$ (MeV) < 12.0	3.13		0.19	
	SF: $80 < E_{SF}$ (MeV) < 300	0.08		0.09	
	E_{ID} (MeV) < 200				
	All events	1800		35	
^{207}Pb	α: $7.85 < E_\alpha$ (MeV) < 8.25	0.70		0.43	
	α: $8.0 < E_\alpha$ (MeV) < 12.0	2.85		0.39	
	All events	1400		32	
^{208}Pb	α: $7.85 < E_\alpha$ (MeV) < 8.25	1.44	0.58	1.04	0.20
	α: $8.0 < E_\alpha$ (MeV) < 12.0	5.06	1.76	1.09	0.50
	All events	1700	990	43	52
^{244}Pu	EVR: $3.0 < E_{EVR}$ (MeV) < 15.0	206	91		
	α: $9.7 < E_\alpha$ (MeV) < 10.2	1.13	0.52	0.05	0.02
	α: $9.0 < E_\alpha$ (MeV) < 9.5	1.40	0.71	0.15	0.07
	α: $8.0 < E_\alpha$ (MeV) < 12.0	10.33	0.53	1.21	0.61
	SF: $80 < E_{SF}$ (MeV) < 400	0.04	0.44	3.31×10^{-4}	8.88×10^{-5}
	E_{ID} (MeV) < 200				
	All events	2900	2084	670	640

after the implantation of the EVR that started the chain. The rate of EVR-like events during the run was 52 s^{-1} (206 s^{-1} inside of the BP) over the entire detector. With this rate, the probability of observing two additional EVRs within the 15 decay chains and in their respective pixels is 17%. Chain 1 also contains an 8.727-MeV α particle that was assigned to the α decay of ^{281}Ds. The rate of α-like events [$8.0 < E_\alpha$ (MeV) < 12.0] during the experiment was 2.29 s^{-1} over the entire detector. The probability that any one of the decay chains had contained a random α-like event is <0.1%. No other additional α-like events were observed in any of the other 14 decay chains.

The original element 114 discovery claim was based on the observation of a 34-min-long EVR-α-α-α-SF chain [19]. We extended our correlation parameters to search for chains of a similar type with α-particle energy windows of 500 keV and lifetime windows three times longer than the lifetimes observed in Ref. [19]. This led to search parameters of EVR-α-α-α-SF correlations consisting of an EVR [$3.0 < E_{EVR}$ (MeV) < 15.0] followed by three subsequent α particles with

(i) $9.5 < E_{\alpha 1}$ (MeV) < 10.0, $\Delta t_{EVR-\alpha 1} < 90$ s,
(ii) $8.4 < E_{\alpha 2}$ (MeV) < 8.9, $\Delta t_{\alpha 1-\alpha 2} < 45$ min,
(iii) $8.6 < E_{\alpha 3}$ (MeV) < 9.1, $\Delta t_{\alpha 2-\alpha 3} < 4.8$ min.

The chain would then have to be terminated by a SF-like event outside of the BP and within 50 min of the last α particle (α3). Unfortunately, with these search conditions, the number of expected random correlations was too high to allow for identification of chains similar to those suggested in Ref. [19], which implies that our experiment was not sensitive to such decay chains.

F. Systematic uncertainties

The systematic uncertainties result from six main contributions: (i) The uncertainty in the efficiency to guide EVRs to the FPD. For the ^{48}Ca + $^{206-208}$Pb reactions, this uncertainty has been estimated to be σ_{eff}/eff = 10% by a comparison of the size and shape of the modeled and experimental focal-plane position distribution. Because the kinematics of the ^{48}Ca + ^{244}Pu reaction are similar, σ_{eff}/eff = 10% was used. (ii) The uncertainty in the target thicknesses. Target thickness measurements were performed for each segment before and after irradiation. They were all integral and do not reflect inhomogeneous microscopic structures of the targets. Loss of target material during the run was estimated to occur during the first several hours of the run, after which, the target thickness remained stable. Errors in the target thickness were estimated to contribute 10% to the systematic uncertainty based on pre- and post-experimental measurements of the target thickness for each individual target. (iii) The uncertainties of the beam doses during the experiment. These were estimated based on readings from an induction coil upstream of the target. The beam dose obtained from the induction coil was then normalized to readings that were periodically taken in a Faraday cup directly upstream of the target. Comparisons of beam intensity as measured in the induction coil and that given by the Faraday cup showed an approximate 6% error. (iv) The Faraday cup is estimated to measure beam intensities to within 5%. (v) Both the Faraday cup and the induction coil are upstream of the target. It is estimated that 95% ± 5% of the beam that passed through the Faraday cup and induction coil also passed through the target. (vi) EVR energy gates were

chosen based on the observed distribution of ^{254,252}No EVRs and the predicted difference between the initial ^{254,252}No and 114 EVR energies as well as the predicted energy losses in the remaining target, MWPC windows, and detector dead layer. ^{254,252}No and 114 EVRs are formed at the center of the target with similar energies. Energy losses of the ^{254,252}No and 114 EVRs were estimated from extrapolation from SRIM2008 of the hypothetical atoms of ^{254}As ($Z = 33$) through ^{254}U ($Z = 92$) to ^{254}No ($Z = 102$) and ^{288}As through ^{288}U to ^{288}114 when passing through the remaining target, Mylar windows of the MWPC, and the dead layer of the FPD. Estimated average ^{254,252}No implantation energies were ∼17% higher than those for 114 EVRs. The energy spread of the 114 EVRs after passing through the remaining target, MWPC windows, and FPD dead layer was also expected to be ∼22% wider than the spread of ^{254}No EVRs. The ^{254,252}No EVRs had an average recorded implantation energy (not corrected for pulse-height defect) of 8.8 MeV with a FWHM of 3.1 MeV. Based on this, the expected 114 EVR implantation energy was 7.1 MeV, with a FWHM of 3.8 MeV. The lower limit for the 114 EVR energy gate was set to 3 MeV because of a large probability of observing random correlations to low-energy noise below 3 MeV. Based on the extrapolations from SRIM2008, 99% ± 5% of the EVR distribution were expected to have energies of $3 \leqslant E_{\mathrm{EVR}}$ (MeV) $\leqslant 15$. Standard error propagation of these six main contributions results in an overall systematic uncertainty of 18% for cross sections measured with TASCA, which is slightly higher than published previously in Ref. [26] because of the inclusion of error from (v) and (vi).

IV. CONCLUSION

The performance of the recently installed gas-filled recoil separator TASCA at the GSI and its new detection system was verified using beams of ^{48}Ca to irradiate targets of $^{206-208}$Pb, which led to the production of $^{252-254}$No isotopes. These studies allowed for the detailed analysis of the performance of the separator and electronics. Decay properties and production rates of the $^{252-254}$No isotopes were in agreement with literature data. In the HTM, the dispersion was determined to be 6.5 mm/(%$B\rho$).

The ^{244}Pu(^{48}Ca,3-4n) reaction was also studied at GSI using the TASCA. Fifteen decay chains were observed and were assigned to ^{288,289}114. The measured half-lives were $0.97^{+0.97}_{-0.32}$, 30^{+30}_{-10} s, 20^{+20}_{-7} s, and 3^{+15}_{-1} ms for ^{289}114, ^{285}Cn, ^{281}Ds, and ^{277}Hs, respectively. For ^{288}114 and its daughters, ^{284}Cn and ^{280}Ds, half-lives of $0.52^{+0.22}_{-0.13}$ s for ^{288}114 and $0.11^{+0.05}_{-0.03}$ s, respectively, were observed. A maximum cross section of $9.8^{+3.9}_{-3.1}$ pb was observed for the 4n evaporation channel at $E^* =$ 39.8–43.9 MeV. While, for the 3n cross section, a maximum of $8.0^{+7.4}_{-4.5}$ pb was observed at $E^* = 36.1$–39.5 MeV. These cross sections and half-lives, as well as decay modes and α-particle energies, agree with those reported from the DGFRS collaboration [23]. The high cross sections and observation of two of the ^{288}114 decay chains in the SIM demonstrate that TASCA is ideal for use as a physical preseparator [59] in future studies of the chemistry of element 114. In addition, we observed a previously unobserved α-decay branch in ^{281}Ds, which led to the discovery of the isotope ^{277}Hs. The separation from TRPs in TASCA was ∼700 in HTM and ∼2000 in SIM.

ACKNOWLEDGMENTS

We thank the ECR ion source and UNILAC staffs for providing excellent and stable ^{48}Ca beams. H. Brand and the GSI Experimental Electronics Department, H. Grösslhuber, G. Matheis, and R. Bühnemann from the machine shop at the Institute of Radiochemistry, TU Munich as well as V. Gorshkov, who provided technical support. L. Stavsetra provided preliminary BGS results for the ^{48}Ca + ^{242}Pu reaction prior to publication, which we gratefully acknowledge. This work was financially supported by the German BMBF (Grants No. 06MT247I, No. 06MT248, and No. 06MZ223I); the Research Center Elementary Forces and Mathematical Foundations (EMG); the GSI-F&E (MT/TÜR, MZJVKR); the Swedish Science Council; the U.S. D.O.E. under Contract No. DE-AC02-05CH11231 and the NNSA under Contract No. DE-FC52-08NA28752; the Norwegian Research Council (Project No. 177538); and the Government of India-XIth 5-year plan project TADDS.

[1] A. Semchenkov *et al.*, Nucl. Instrum. Methods Phys. Res. B **266**, 4153 (2008).
[2] K. Morita *et al.*, J. Phys. Soc. Jpn. **73**, 2593 (2004).
[3] J. Khuyagbaatar (to be published).
[4] A. Gorshkov (to be published).
[5] A. Gorshkov, Doktors der Naturwissenschaften (Dr. rer. nat.) thesis, Technische Universität München, 2010.
[6] Y. T. Oganessian *et al.*, Phys. Rev. C **64**, 054606 (2001).
[7] K. E. Gregorich *et al.*, Phys. Rev. C **72**, 014605 (2005).
[8] J. B. Patin, *Lawrence Berkeley National Laboratory Report No. LBNL-49593*, 2002 (unpublished).
[9] J. M. Nitschke, R. E. Leber, M. J. Nurmia, and A. Ghiorso, Nucl. Phys. A **313**, 236 (1979).
[10] R.-D. Herzberg *et al.*, Nature (London) **442**, 896 (2006).
[11] S. K. Tandel *et al.*, Phys. Rev. Lett. **97**, 082502 (2006).
[12] H. W. Gäggeler *et al.*, Nucl. Phys. A **502**, 561 (1989).
[13] B. Sulignano *et al.*, Eur. Phys. J. A **33**, 327 (2007).
[14] F. Heßberger *et al.*, Eur. Phys. J. A **43**, 55 (2010).
[15] A. V. Belozerov *et al.*, Eur. Phys. J. A **16**, 447 (2003).
[16] F. P. Heßberger, S. Hofmann, D. Ackermann, P. Cagarda, R.-D. Herzberg, I. Kojouharov, P. Kuusiniemi, M. Leino, and R. Mann, Eur. Phys. J. A **22**, 417 (2004).
[17] L.-L. Andersson *et al.*, Nucl. Instrum. Methods Phys. Res. A **622**, 164 (2010).
[18] Y. T. Oganessian *et al.*, Phys. Rev. C **69**, 054607 (2004).
[19] Y. T. Oganessian *et al.*, Phys. Rev. Lett. **83**, 3154 (1999).
[20] Y. T. Oganessian *et al.*, Phys. Rev. C **62**, 041604 (2000).
[21] Y. T. Oganessian *et al.*, Phys. Rev. C **63**, 011301 (2000).

[22] Y. T. Oganessian *et al.*, Phys. Rev. C **70**, 064609 (2004).
[23] Y. T. Oganessian, J. Phys. G **34**, R165 (2007).
[24] L. Stavsetra, K. E. Gregorich, J. Dvorak, P. A. Ellison, I. Dragojevic, M. A. Garcia, and H. Nitsche, Phys. Rev. Lett. **103**, 132502 (2009).
[25] P. A. Ellison *et al.*, Phys. Rev. Lett. **105**, 182701 (2010).
[26] C. E. Düllmann *et al.*, Phys. Rev. Lett. **104**, 252701 (2010).
[27] K. Eberhardt *et al.*, Nucl. Instrum. Methods Phys. Res. A **590**, 134 (2008).
[28] J. F. Ziegler, Nucl. Instrum. Methods Phys. Res. B **219-220**, 1027 (2004).
[29] G. Audi, O. Bersillon, J. Blachot, and A. H. Wapstra, Nucl. Phys. A **729**, 3 (2003).
[30] W. D. Myers and W. J. Świątecki, *Lawrence Berkeley National Laboratory Report No. LBNL-36803*, 1994.
[31] K. E. Gregorich *et al.*, Eur. Phys. J. A **18**, 633 (2003).
[32] K. E. Gregorich *et al.*, *GSI Helmholtzzentrum für Schwerionenforschung Report No. NUSTAR-SHE-10*, 2006.
[33] J. P. Biersack and L. G. Haggmark, Nucl. Instrum. Methods **174**, 257 (1980).
[34] J. Eberth, H. G. Thomas, P. v. Brentano, R. M. Lieder, H. M. Jäger, H. Kämmerfing, M. Berst, D. Gutknecht, and R. Henck, Nucl. Instrum. Methods Phys. Res. A **369**, 135 (1996).
[35] *Table of Isotopes*, edited by R. B. Firestone and V. S. Shirley (Wiley, New York, 1996).
[36] V. E. Viola and G. T. Seaborg, J. Inorg. Nucl. Chem. **28**, 741 (1966).
[37] V. E. Viola, K. Kwiatkowski, and M. Walker, Phys. Rev. C **31**, 1550 (1985).
[38] H. Kudo, Workshop on Recoil Separator for Superheavy Element Chemistry (unpublished).
[39] C. E. Bemis, R. L. Ferguson, F. Plasil, R. J. Silva, F. Pleasonton, and R. L. Hahn, Phys. Rev. C **15**, 705 (1977).
[40] J. F. Wild, E. K. Hulet, R. W. Lougheed, K. J. Moody, B. B. Bandong, R. J. Dougan, and A. Veeck, J. Alloy. Comp. **213-214**, 86 (1994).
[41] A. N. Andreyev, D. D. Bogdanov, V. I. Chepigin, A. P. Kabachenko, O. N. Malyshev, R. N. Sagaidak, L. I. Salamatin, G. M. Terakopian, and A. V. Yeremin, Z. Phys. A **345**, 389 (1993).
[42] A. Türler, GSI Report No. 1989 (unpublished).
[43] Y. T. Oganessian, V. K. Utyonkov, and K. J. Moody, Phys. At. Nucl. **64**, 1349 (2001).
[44] J. Dvorak *et al.*, Phys. Rev. Lett. **97**, 242501 (2006).
[45] J. Dvorak *et al.*, Phys. Rev. Lett. **100**, 132503 (2008).
[46] R. Smolańczuk, J. Skalski, and A. Sobiczewski, Phys. Rev. C **52**, 1871 (1995).
[47] R. Smolańczuk, Phys. Rev. C **56**, 812 (1997).
[48] I. Muntian, Z. Patyk, and A. Sobiczewski, Phys. Lett. B **500**, 241 (2001).
[49] K. Morita *et al.*, Eur. Phys. J. A **21**, 257 (2004).
[50] S. Hofmann *et al.*, Eur. Phys. J. A **10**, 5 (2001).
[51] S. Hofmann Rep. Prog. Phys. **61**, 639 (1998).
[52] F. P. Heßberger *et al.*, Eur. Phys. J. A **41**, 145 (2009).
[53] I. Dragojević, K. E. Gregorich, C. E. Düllmann, J. Dvorak, P. A. Ellison, J. M. Gates, S. L. Nelson, L. Stavsetra, and H. Nitsche, Phys. Rev. C **79**, 011602(R) (2009).
[54] C. M. Folden III, K. E. Gregorich, C. E. Düllmann, H. Mahmud, G. K. Pang, J. M. Schwantes, R. Sudowe, P. M. Zielinski, H. Nitsche, and D. C. Hoffman, Phys. Rev. Lett. **93**, 212702 (2004).
[55] W. Brüchle, Radiochim. Acta **91**, 71 (2003).
[56] H. Gäggeler *et al.*, Phys. Rev. C **33**, 1983 (1986).
[57] G. Guarino, A. Gobbi, K. D. Hildenbrand, W. F. J. Müller, A. Olmi, H. Sann, S. Bjørnholm, and G. Rudolf, Nucl. Phys. A **424**, 157 (1984).
[58] J. Tøke *et al.*, Nucl. Phys. A **440**, 327 (1985).
[59] C. E. Düllmann, C. M. Folden III, K. E. Gregorich, D. C. Hoffman, D. Leitner, G. K. Pang, R. Sudowe, P. M. Zielinski, and H. Nitsche, Nucl. Instrum. Methods Phys. Res. A **551**, 528 (2005).